Singularity Analysis and Solutions for the Origami Transmission Mechanism of Fast-Moving Untethered Insect-Scale Robot

Yide Liu, Bo Feng, Tianlun Cheng, Yanhong Chen, Xiyan Liu, Jiahang Zhang, Shaoxing Qu, *Member, IEEE*, and Wei Yang

***Abstract*—Designing insect-scale robots with high mobility is becoming an essential challenge in the field of robotics research. Among the methods for fabricating the transmission mechanism of the insect-scale robot, the smart composite microstructure (SCM) method is getting more and more attention. This method can construct compact and functional miniature origami mechanisms through planarized fabrication and folding assembly processes. Our previous work has proposed an untethered robot S^2worm equipped with a novel 2-DoF origami transmission mechanism. The S^2worm is fabricated through SCM and holds a top speed of 27.4 cm/s. In this work, we propose a novel strategy for designing the insect-scale robot with high mobility, that is, applying Grassmann–Cayley Algebra (GCA) to avoid the singularity of the transmission mechanism. The experimental results prove that the singularity of the previous work has been solved. The new robot prototype S^2worm-G weighs 4.71 g, scales 4.0 cm, achieves a top speed of 75.0 cm/s and a relative speed of 18.8 bodylength/s. To the best of our knowledge, the 2-DoF origami transmission mechanism is the first parallel mechanism designed for the insect-scale robot and the singularity of the mechanism is found and solved here. The experimental results prove that the refined S^2worm-G robot is one of the best insect-scale robots for its size, mass, and mobility.**

***Index Terms*—Grassmann–Cayley algebra (GCA), insect-scale robot, origami transmission mechanism, singularity, smart composite microstructure (SCM).**

I. Introduction

THE insect-scale robot is a type of robot with small scale, low weight, and high mobility. These robots hold high expectations for applications, such as confined space inspection, earthquake search, and planetary exploration. All these potential applications make demands on the mobility and autonomy of the robot design. During the last two decades, many researchers investigated the design principle and the fabrication method of the insect-scale robot.

Unlike traditional robots commonly consisting of motors, links, and bearings, insect-scale robots mainly apply microfabrication technologies and off-the-shelf components. Generally, millimeter-scale mechanisms and smart materials are employed as robot bodies and actuators, respectively. The smart materials can be classified mainly as: electroactive materials such as piezoelectric ceramic [1], [2] and dielectric elastomer [3], [4], and thermal active materials such as shape memory alloy [5], [6], [7], [8] and polymer [9]. Though this smart material actuator holds advantages including small size, lightweight, and high integration, the output force and displacement are relatively small. Moreover, smart material actuators generally perform deformation rather than pure rotation or translation motion like motors. In this situation, it requires the robot body to play the role not only of supporting the robot components as chassis, but also as transmission to convert the output of the smart material actuators [10], [11]. This needs the robot body to be designed not only small and compact, but also functional.

Many methods are proposed for designing small transmission mechanism such as smart composite microstructure (SCM) method [12], [13], silicon on insulator process [14], 3-D printing [15], etc. Among all these methods, SCM gets more and more attention for its successful application in many robot prototypes, such as Dash [16], HAMR series [2], [17], and some other terrestrial robots [8], [18], [19], micro flapping-wing robots [1], [20], [21], [22], small parallel robots [23], [24], [25], [26], etc. The SCM method allows the designer to construct a lightweight structure and complex transmission mechanism through origami and pop-up strategies [27]. Flexible and compact mechanisms can be fabricated without redundant assembly processes but only through folding and connecting from a 2-D structure.

However, this type of folding fabrication process often leads to the singularity of the robot since the flexure joints employed by SCM are fabricated flattened. Most joints have a natural point of about zero degrees, which may make the initial configuration of the robot become a singular state. The transmission mechanism at singular configuration loses the stiffness and gains some

Manuscript received 4 September 2023; revised 12 November 2023; accepted 23 November 2023. Date of publication 4 December 2023; date of current version 29 December 2023. This paper was recommended for publication by Associate Editor L. Zhang and Editor A. Menciassi upon evaluation of the reviewers' comments. This work was supported in part by the National Natural Science Foundation of China under Grant 91748209, in part by the 111 Project under Grant B21034, and in part by the Key Research and Development Program of Zhejiang Province under Grant 2021C01183. *(Corresponding author: Shaoxing Qu.)*

The authors are with the State Key Laboratory of Fluid Power and Mechatronic System, Key Laboratory of Soft Machines and Smart Devices of Zhejiang Provinces, Center for X-Mechanics, Department of Engineering Mechanics, Zhejiang University, Hangzhou 310027, China (e-mail: yide_liu@zju.edu.cn; 12124023@zju.edu.cn; 22160087@zju.edu.cn; 3150100917@zju.edu.cn; dipsy@zju.edu.cn; zjh2378@163.com; squ@zju.edu.cn; yangw@zju.edu.cn).

This article has supplementary downloadable material available at https://doi.org/10.1109/TRO.2023.3338949, provided by the authors.

Digital Object Identifier 10.1109/TRO.2023.3338949

unwanted degree(s) of freedom (DoF). This turns to the singularity analysis of the mechanism, which is a classic problem in the field of the parallel robot. Many strategies have been proposed to solve the singularity problem. Gosselin and Angeles classified the singularities of closed-loop mechanisms by considering two Jacobians that define the relationship between input and output velocities [28]. Merlet analyzed the singularities of the 6-DoF Gough–Stewart platform through Grassmann geometry (GG) [29]. Ben-Hori and Shoham applied Grassmann-Cayley algebra (GCA) to a type of 6-DOF parallel robot that has connectivity six between the base and the moving platform [30]. Plenty of works demonstrated the importance of singularity analysis to the performance of the parallel mechanism. Although SCM has been applied in many projects for fabricating origami transmission mechanism and the singularity problems of the origami transmission mechanism may restrict the performance of the robot, the singularity problems of the SCM structure does not hold enough attention. We tend to attribute this phenomenon to the insect-scale robot is a relatively new topic and few parallel mechanisms are designed for insect-scale mobile robot transmission specifically.

To fill this gap, our previous work proposed a novel 2-DoF origami transmission mechanism through screw theory and type synthesis method for the insect-scale robot to achieve universal locomotion. The robot is fabricated through the SCM method and named S^2worm [19]. Even though the robot performs relatively high mobility such as 27.4 cm/s top speed and 1.7 cm turning radius, the experiments still reveal some problems. For instance, the velocity of the robot is still below expectation and the turning speed of the robot is much lower than the forward locomotion speed. We attribute these flaws to the singularity problems of the 2-DoF origami transmission mechanism we designed.

This work aims to propose a novel strategy for designing the insect-scale robot with high mobility, that is, applying GCA to avoid the singularity of the transmission mechanism. In this article, we focus on optimizing the transmission mechanism of the insect-scale mobile robot fabricated through the SCM method. We demonstrate the singularity of the transmission mechanism in our previous design through the stiffness test and slow-motion video. We perform an exhaustive singularity analysis of the 2-DoF origami transmission mechanism through the GCA calculation. The singular conditions of GCA calculation are connected with the geometry of the mechanism. The SCM design is refined based on the GCA calculation. The new prototype is named S^2worm-G for short.

Experimental results show that the new design based on the GCA calculation of the 2-DoF origami transmission mechanism completely solves the singularity problem compared with the previous design. The mobility of the S^2worm-G is greatly improved. The forward locomotion velocity raises from 27.4 to 75.0 cm/s. The turning velocity raises from $\sim$1.2 to 9.3 cm/s. The mobility improvement of the S^2worm-G proves that the GCA can guide the design of the SCM fabricated structure and optimize the performance of the transmission through the singularity analysis. Following the processes we propose, the 2-DoF origami transmission mechanism can be applied in other insect-scale robots as high performance transmission mechanism. This work also proves that the type synthesis method (our previous work) and the GCA calculation (this work) is a feasible route for the insect-scale robot with SCM made origami structure.

The rest of this article is organized as follows. Section II describes the S^2worm-G robot, which includes: the general description of the S^2worm-G, the kinematic design of the 2-DoF origami transmission mechanism, the principle of the transmission mechanism and the locomotion of the robot, limitations in the SCM method, and the phenomena of the singularities in the previous S^2worm. Section III gives the singularity analysis of the 2-DoF origami transmission mechanism through GCA, which includes the constraint wrench system, the actuation wrench system, and the overall wrench system of the mechanism in a symbolic form, the calculation and the decomposition process. The geometric entities of the algebraic formulas are illustrated, and the singularity of our previous design is analyzed. Section IV explains the design and fabrication of the refined SCM structure, the fabrication of the actuator and the control circuit design. In Section V, experimental setup and results on the singularities of the 2-DoF origami transmission mechanism and the S^2worm-G robot are reported. Finally, Section VI concludes this article.

II. System Description

A. General Description of the Robot

S^2worm [19] is a project for building insect-scale inchworm robots with a 2-DoF origami transmission mechanism fabricated by SCM method. S^2worm can be separated into several subsystems: the driving system, the power system and the control system. The driving system includes the piezoelectric actuator, the slider-crank mechanisms, and the 2-DoF origami transmission mechanism. The power system includes the battery and the high voltage boost converter. The control system is a control board equipped with a microprocessor. All these subsystems are integrated thus the robot achieves power and control autonomy. To balance the mass distribution of the robot, the control devices and the high voltage boost converter are attached to the front of the robot, the battery and the actuator are attached to the rear of the robot.

The robot is driven by a double deck piezoelectric actuator. The actuation is generated through the electro–mechanical properties of the piezoelectric ceramic (PZT). High voltages are applied on the surface of the PZT which causes the piezoelectric actuator to perform a deflection at the tip. Slider-crank mechanisms are introduced between the piezoelectric actuator and the 2-DoF origami transmission mechanism, which transfers the deflection of the actuator into the rotation of the actuation joint of the mechanism.

The previous S^2worm [19] can perform untethered locomotion with the top average speed of 27.4 cm/s. The speed and the untethered properties make S^2worm become one of the best insect-scale robots. Besides, the novel 2-DoF origami transmission mechanism we designed through screw theory and type synthesis shows great potential as the transmission mechanism of the insect-scale robot.

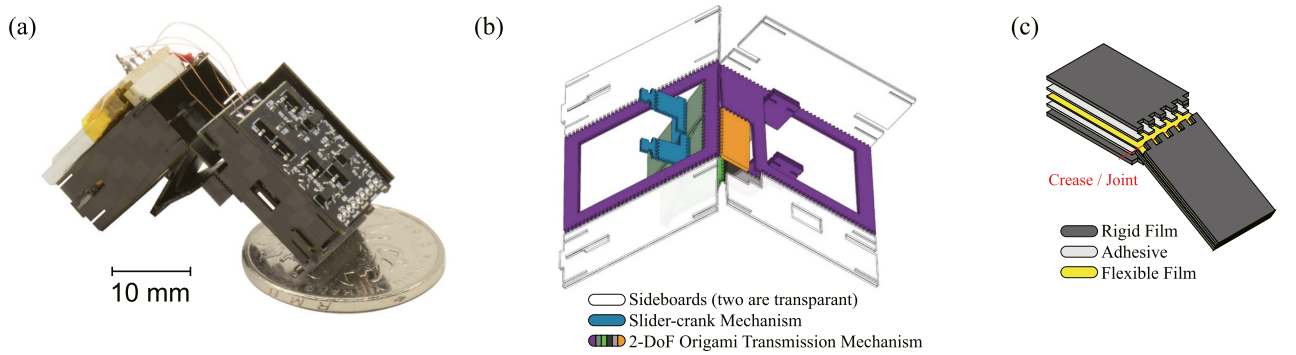

Fig. 1. (a) Photograph of the S^{2}worm-G. A coin is included for scale. (b) The CAD model of the SCM structure of the S^{2}worm-G. The model includes the 2-DoF origami transmission mechanism, four sideboards and two slider-crank mechanisms. (c) The principle of a joint in the SCM structure. A flexible film sandwiched by adhesive and two rigid films. The rigid films form the link. The "castle" crease and the flexible film form the joint. Constrained by the "castle" crease, the range of the SCM joint is $[-90, +90]^\circ$.

In this article, the second generation of the S^{2}worm is performed, named S^{2}worm-G (see Fig. 1). Compared with the previous work, the appearance and weight of the robot are almost unchanged (S^{2}worm: 4.1 cm, 4.34 g; S^{2}worm-G: 4.0 cm, 4.71 g). The new prototype mainly improves the 2-DoF origami transmission mechanism with the instruction of the singularity analysis by GCA. This improvement leads to large a promotion of the mobility of the robot. Attributed to the singularity analysis, the new design avoids the singular configuration. The top speed of the S^{2}worm-G achieves 75.0 cm/s and the turning speed achieves 9.3 cm/s.

B. Kinematic Design of the 2-DoF Origami Transmission Mechanism

In this article, we mainly focus on the singularity analysis of the 2-DoF origami transmission mechanism of the S^{2}worm-G [see Fig. 1(b)]. Based on the previous work [19], the type synthesis and mobility analysis of the transmission mechanism are performed. The 2-DoF origami transmission mechanism with the notations is illustrated in Fig. 2 and the list of symbols used in this article is given in Table I. The 2-DoF origami transmission mechanism is a parallel mechanism with three limbs, an exoskeleton limb, and two muscle limbs. Exoskeleton limb contains joints S_{11} and S_{12}, muscle limbs contain S_{21} to S_{25} and S_{31} to S_{35} [see Fig. 2(c)].

The exoskeleton limb contains two intersecting revolute joints, which can be assimilated to a universal joint. The muscle limbs contain five revolute joints. The first three revolute joints are parallel to each other and the last two revolute joints are parallel to each other, respectively, thus the limb can be denoted by $\overline{\mathrm{RRR}}\underline{\mathrm{RR}}$. Two actuation joints are selected as the first joint of the muscle limbs S_{21} and S_{31} [see Fig. 2(c)]. The geometry notation of the mechanism is defined in the affine space, the points of joints on the limbs are labeled from A_1 to D_3. Point O is chosen as the origin of the mechanism. Direction vectors $\boldsymbol{e_1}$ and $\boldsymbol{e_2}$ are the direction vectors of the first joint and second joint of the exoskeleton limb, respectively. Direction vector $\boldsymbol{e_3}$ is defined as $\boldsymbol{e_3} = \boldsymbol{e_1} \times \boldsymbol{e_2}$. Direction vectors $\boldsymbol{p_2}$, $\boldsymbol{v_2}$, $\boldsymbol{p_3}$, and $\boldsymbol{v_3}$ are defined along the link B_2C_2, C_2D_2, B_3C_3, and C_3D_3, respectively.

Five planes $\mathscr{P}_2$, $\mathscr{V}_2$, $\mathscr{P}_3$, $\mathscr{V}_3$, and $\mathscr{M}$ are defined based on the limb geometry. $\mathscr{P}_i (i = 2, 3)$ describe the plane pass the point $C_i (i = 2, 3)$ with the normal vector $\boldsymbol{p_i} \times \boldsymbol{e_1} (i = 2, 3)$. $\mathscr{V}_i (i = 2, 3)$ describes the plane passes the point $C_i (i = 2, 3)$ with the normal vector $\boldsymbol{v_i} \times \boldsymbol{e_2} (i = 2, 3)$. Plane $\mathscr{M}$ is the plane pass the point A_1 with the normal vector $\boldsymbol{e_3}$.

The twist system of the exoskeleton limb is written as

$$\mathbb{S}_1 = \begin{Bmatrix} \mathrm{S}_{11} & = (\boldsymbol{e_1}; \boldsymbol{r_{A_1}} \times \boldsymbol{e_1}) \\ \mathrm{S}_{12} & = (\boldsymbol{e_2}; \boldsymbol{r_{A_1}} \times \boldsymbol{e_2}) \end{Bmatrix} \tag{1}$$

where $\boldsymbol{r_{A_1}}$ is the position vector of the point A_1.

The twist systems of the muscle limbs are written as

$$\mathbb{S}_i = \begin{Bmatrix} \mathrm{S}_{i1} & = (\boldsymbol{e_1}; \boldsymbol{r_{A_i}} \times \boldsymbol{e_1}) \\ \mathrm{S}_{i2} & = (\boldsymbol{e_1}; \boldsymbol{r_{B_i}} \times \boldsymbol{e_1}) \\ \mathrm{S}_{i3} & = (\boldsymbol{e_1}; \boldsymbol{r_{C_i}} \times \boldsymbol{e_1}) \\ \mathrm{S}_{i4} & = (\boldsymbol{e_2}; \boldsymbol{r_{C_i}} \times \boldsymbol{e_2}) \\ \mathrm{S}_{i5} & = (\boldsymbol{e_2}; \boldsymbol{r_{D_i}} \times \boldsymbol{e_2}) \end{Bmatrix} (i = 2, 3). \tag{2}$$

According to the previous work, the inputs of the double deck piezoelectric actuator are introduced at the twists S_{21} and S_{31} through the slider-crank mechanisms.

The lift and twist motions of the transmission mechanism correspond to the rotations of the moving platform about the joints S_{11} and S_{12} [see Fig. 2(d)]. These two motions generate the forward and the turning motions of the robot, respectively. The kinematics of the 2-DoF origami transmission mechanism is demonstrated in Supplementary Movie S1.

C. Principle of the Lift and Twist Motion

To demonstrate the lift and twist motion, we simplify the robot as two boxes connected by a universal joint (see Fig. 3). The universal joint allows the front to perform a 2-DoF rotation with respect to the rear. The boxes represent the front and the rear of the S^{2}worm-G robot, respectively. The actuation forces generated by the muscle limbs are simplified as two arrows. This simplification can be proved by the actuation wrenches of the muscle limbs in the following derivation [see (9)].

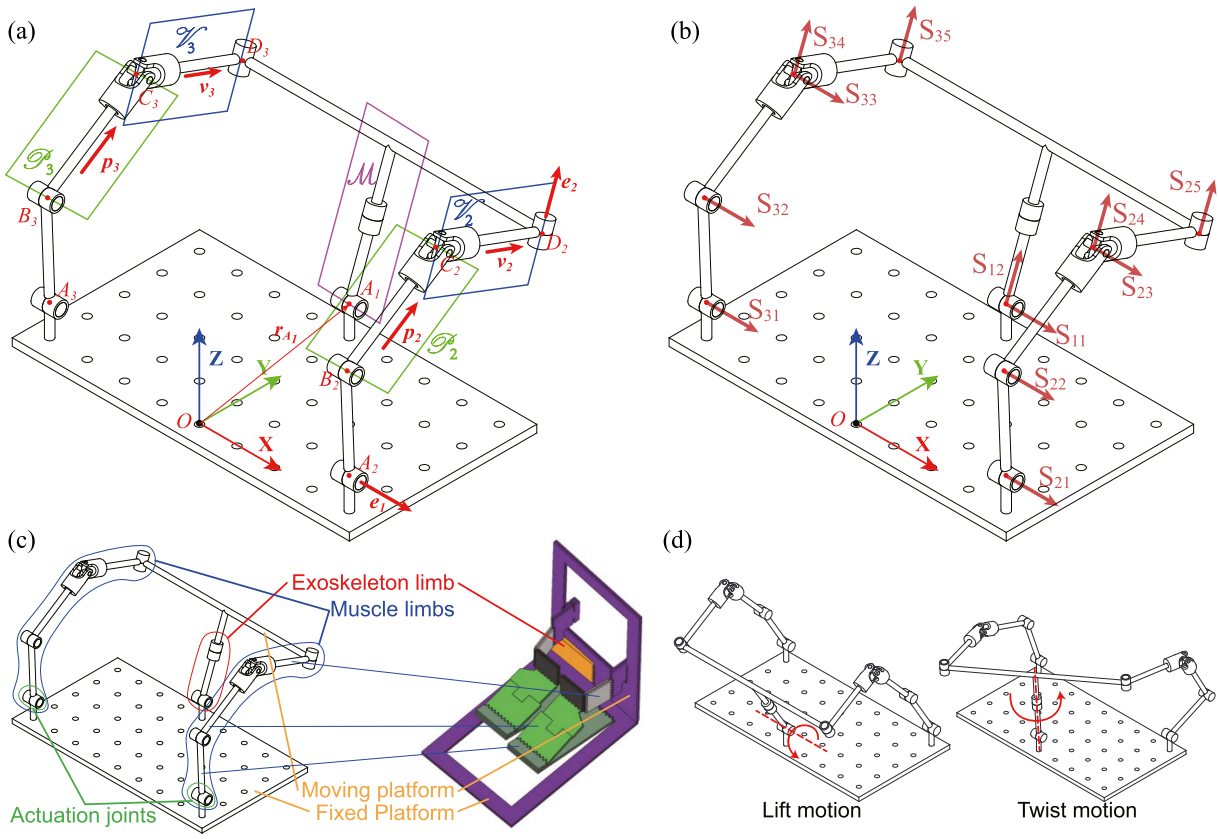

Fig. 2. Schematic of the 2-DoF origami transmission mechanism. (a) Geometry notation. (b) Screw notation. (c) Limb notation and links correspondence. (d) Lift and twist motion.

TABLE I
SYMBOL TABLE OF THIS ARTICLE

	Type	Symbol
Affine Space	Point	$O, A_1, A_2, A_3, B_2, B_3, C_2, C_3, D_2, D_3$
	Vector	$\boldsymbol{e_1}, \boldsymbol{e_2}, \boldsymbol{e_3}, \boldsymbol{p_2}, \boldsymbol{v_2}, \boldsymbol{p_3}, \boldsymbol{v_3}, \boldsymbol{s_2}, \boldsymbol{s_3}, \boldsymbol{r_{A_1}}\text{-}\boldsymbol{r_{D_3}}$
	Plane	$\mathscr{P}_2, \mathscr{P}_3, \mathscr{V}_2, \mathscr{V}_3, \mathscr{M}$
Screw	Screw System	$\mathbb{S}_1, \mathbb{S}_2, \mathbb{S}_3, \mathbb{S}_c, \mathbb{S}_a$
	Twist	$\mathrm{S}_{11}, \mathrm{S}_{12}, \mathrm{S}_{21}, \mathrm{S}_{22}, \mathrm{S}_{23}, \mathrm{S}_{24}, \mathrm{S}_{25}, \mathrm{S}_{31}, \mathrm{S}_{32}, \mathrm{S}_{33}, \mathrm{S}_{34}, \mathrm{S}_{35}$
	Wrench	$\mathrm{S}^r_{11}, \mathrm{S}^r_{12}, \mathrm{S}^r_{13}, \mathrm{S}^r_{14}, \mathrm{S}^r_{21}, \mathrm{S}^r_{31}, \mathrm{S}_{c1}, \mathrm{S}_{c2}, \mathrm{S}_{c3}, \mathrm{S}_{c4}, \mathrm{S}_{a1}, \mathrm{S}_{a2}$
Projective Space	Finite Point	$\mathrm{A}_1, \mathrm{C}_2, \mathrm{C}_3$
	Infinite Point	$\underline{\mathrm{e}}_1, \underline{\mathrm{e}}_2, \underline{\mathrm{e}}_3, \underline{\mathrm{p}}_2, \underline{\mathrm{p}}_3, \underline{\mathrm{v}}_2, \underline{\mathrm{v}}_3, \underline{\mathrm{s}}_2, \underline{\mathrm{s}}_3$
	Line	$\mathrm{S}_{c1}, \mathrm{S}_{c2}, \mathrm{S}_{c3}, \mathrm{S}_{c4}, \mathrm{S}_{a1}, \mathrm{S}_{a2}$ (same as wrench)

The lift motion is achieved by actuating the muscle limbs synchronously. At this condition, the two actuation forces exhibit a pure mirror symmetry and the net force makes the front rotates along the transverse axis of the universal joint.

The twist motion is driven by the muscle limbs asynchronously. At this condition, the two actuation forces form a torque applied on the front beside the lift force, which makes the front perform rotation along the vertical axis of the universal joint. It is worthwhile to mention that even though the two muscle limbs are driven out of phase, the front will still lift slightly since the net lift force is hard to offset. This is the parasitic lift motion during the twist motion.

D. Principle of the Forward Locomotion

The forward locomotion of the insect-scale mobile robot can be achieved by gait or directional friction. Special foot structures are often used in inchworm robots to generate directional friction [8], [31]. While the S^{2}worm-G in this work is not equipped with any directional friction structure, its forward motion is generated by the lift motion of the driving mechanism. During the lift motion cycle, the asymmetrical normal force causes asymmetrical friction, which forms the propulsion of the forward motion of the S^{2}worm-G robot. This phenomenon is similar to the two-anchor crawling motion [32] and we separate the locomotion cycle into two phases, the push phase and the

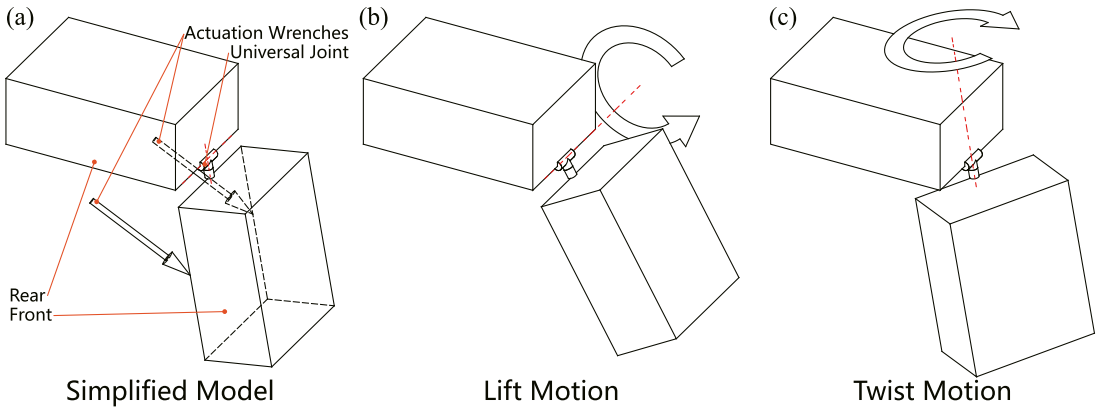

Fig. 3. (a) Simplified model of the S ^{2} worm series robots. (b) The principle of the lift motion. The resultant force of the actuation forces makes the front rotate along the transverse axis of the universal joint. (c) The principle of the twist motion. The resultant force of the actuation forces is torque plus a force. The torque rotates the front along the vertical axis and the force generates the parasitic lift motion.

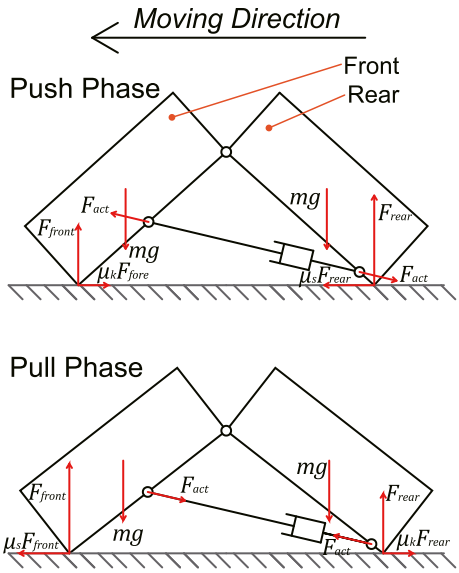

Fig. 4. Principle of forward locomotion. The robot can be simplified as two boxes, front and rear, with equal mass. The actuation wrenches can be simplified as a virtual linear actuator connected between the front and rear.

pull phase (see Fig. 4). Since the two actuation wrenches are symmetric during the forward motion, the robot is simplified as a virtual linear actuator connecting the front and the rear. According to the mass distribution (see Table VII), the mass of the front and rear are considered to be equal and the mass of the virtual linear actuator is neglected. During the push phase, the virtual linear actuator generates push force. The vertical component of the actuator exerts a lift force on the front while pressing the rear. During the push phase, the force of the ground can be written as

$$\begin{aligned} F_{\text{front}} &= \text{mg} - F_{\text{act}}^{v} \\ F_{\text{rear}} &= \text{mg} + F_{\text{act}}^{v} \end{aligned} \tag{3}$$

where F_{front} and F_{rear} are the normal force of the front and the rear, m is the mass of the front and rear, g is the gravity acceleration, and F_{act}^{v} is the vertical component of the driving force generated by the virtual linear actuator.

The friction state during the push phase can be written as

$$\begin{aligned} \mu_s F_{\text{front}} &< \mu_s F_{\text{rear}} \\ \mu_k F_{\text{front}} &< F_{\text{act}}^{H} < \mu_s F_{\text{rear}} \end{aligned} \tag{4}$$

where μ_s and μ_k are the static and kinetic coefficients of the friction, and F_{act}^{H} is the horizontal component of the driving force of the virtual linear actuator.

During the pull phase, the virtual linear actuator generates pull force. The vertical component of the actuator exerts a lift force on the rear while pulling back the front. The force analysis can be written as

$$\begin{aligned} F_{\text{front}} &= \text{mg} + F_{\text{act}}^{v} \\ F_{\text{rear}} &= \text{mg} - F_{\text{act}}^{v} \\ \mu_s F_{\text{rear}} &< \mu_s F_{\text{front}} \\ \mu_k F_{\text{rear}} &< F_{\text{act}}^{H} < \mu_s F_{\text{front}}. \end{aligned} \tag{5}$$

According to (4) and (5), the rear of the robot sticks on the ground as a stance and the front moves forward during the pull phase, while the front works as stance and the rear slips forward during the pull phase. Based on this locomotion cycle, the robot moves forward in both phases.

It is observed in the slow-motion video (see Supplementary Movie S2) that the front of the robot may lift in mid-air in the push phase. In (3), $\text{mg} \leq F_{\text{act}}^{v}$ will lead to the front of the robot leaving the ground. This phenomenon is more common in the S^{2}worm-G since the refined transmission mechanism is more powerful. In the S^{2}worm-G, the forward locomotion is mainly generated by the push phase rather than both phases. For most pull phases, the front of the robot is in the air and cannot contact with the ground to generate propulsion.

The turning is achieved by the twist motion of the mechanism. Due to the twist of the robot's body, the direction of the propulsion does not coincide with the robot's direction, which leads to the robot making turns. In experiments, the turning is

achieved by driving the decks of the piezoelectric actuator with different frequencies.

E. Two Limitations in the SCM

The transmission mechanism is fabricated through the SCM method, which is one of the most popular fabrication methods in small-scale robots. It has significant potential in building high-performance transmission mechanisms because it can fabricate complex and compact structures from 2-D films and further assemble them by folding. However, this method also has some intrinsic limitations that have not yet received enough attention.

Here, we conclude two limitations that lie in the fabrication and assembly process. SCM structures are fabricated from films through laser cutting and heat pressing [12], [13]. After fabrication, the whole structure is 2-D, all links are connected through the flexible film. The rigid films form the links. The "castle" crease and the flexible film form the joint [see Fig. 1(c)]. The assembly process is "pop-up," which includes folding selected creases and bonding links to form a 3-D closed loop structure [13]. These specific processes lead to some limitations, which are concluded as follows.

1) *Connectivity in Design:* All links must be connective. Creases are patterned on the rigid films while all the rigid films are adhesive on the flexible film. Thus, the structure can only contain revolute joints rather than prismatic joints, which brings constraints in limb design. This limitation has been solved in our previous paper [19]. We demonstrated that the screw algebra can be applied to choose the appropriate limb twist space to form the mechanism without a prismatic joint.
2) *Singularity in Pop-Up Assembly:* Pop-up process must avoid the singular configurations. After fabrication, all links and joints are coplanar. From this initial state, the mechanism is easy to meet singular configuration. This can be mitigated if the mechanism design and the pop-up process can follow the singularity analysis.

The singularity of the SCM structures follows the definition of parallel mechanism. The mechanism will gain or lose one or more DoFs at its singular configurations [29], [33]. More specifically, singularity can be classified as transmission singularity and constraint singularity, loss of control and weak stiffness are both typical phenomena of singular conditions, respectively. As for the origami transmission mechanism of the S^2worm, the singularity phenomena on the lift motion and twist motion will decrease the mobility of the forward and turning locomotion.

F. Demonstrations of the Singularity

Taking the previous 2-DoF origami transmission mechanism as an example, we captured the phenomena of singularity in this mechanism. The loss of control of the transmission mechanism is recorded by the slow-motion video in Supplementary Movie S3. It is shown that, under high driving frequencies (90 Hz and above), the muscle limbs will shake while the moving platform does not perform lift or twist motion.

The other phenomenon of the singularity is the weak stiffness in the locked structure. The actuation joints are locked to the fixed platform, this condition can be considered as extremely large actuation torques applied on these joints. The stiffness tests (see Supplementary Movie S4) are performed to prove the weak stiffness in the previous design and the large stiffness improvement after solving the singularity, further data collection, and calculation are provided in Section V-A. Supplementary Movie S5 demonstrated the weak stiffness in detail. Even after locking the actuation joints, the moving platform can still be manipulated by hand easily. These indicate that the actuation torques can not support the moving platform under external payload, thus it is still a characteristic of the transmission singularity rather than the constraint singularity.

The target of this article is to reveal the singularity in the SCM structures, we further demonstrate how much performance of the robot can promote by solving the singularity. We apply the GCA to analyze the singularity of the 2-DoF origami transmission mechanism and guide the structure design. To mathematically evaluate the improvement of the singularity analysis, a coordinate-free dimensionless index local singularity index (LSI) [33] is introduced to compare the closeness to singularities of the previous and refined origami transmission mechanism (see Section IV-B).

III. Singularity Analysis of the 2-DoF Origami Transmission Mechanism

In Sections II-E and II-F, we define the singularity in SCM structures. We further analyze the causes and negative effects of the singularity of the 2-DoF origami transmission mechanism. In this section, we solve the singularities of the mechanism through GCA.

Several methods are composed for the singularity analysis such as: calculating the determinant of the Jacobian matrix, GG, and GCA. Here, we prefer to apply GCA rather than the other two approaches to guide the SCM design for the following motivations.

1) The SCM method is seldom applied in constructing parallel mechanisms with six DoFs. Most of the SCM structures, including the 2-DoF origami transmission mechanism we solved in this work, are low-mobility parallel mechanisms (DoF less than six). For this type of mechanism, the Jacobian matrix is hard to derive.
2) SCM is a compliant mechanism based method. Most of the parallel mechanisms fabricated by SCM contain only the revolute joints (besides the Sarrus mechanism which can perform translation as a prismatic joint).
   Actuation joints of the SCM structure are seldom fabricated as the prismatic joint. Generally, GG prefers the condition that actuation joints are prismatic joints for easily identifying the actuation wrenches. In SCM structure, lots of revolute joints lead to difficulties in solving the actuation wrenches, which will be an inconvenience for GG approaches.
3) We can find all the possible singular configurations through the GCA calculation by connecting the configuration of the mechanism in affine space and the GCA statement in projective space. The results of GCA can guide us to estimate whether a configuration is singular. This is helpful during the SCM design process.

The roots of GCA come from the exterior algebra created by Herman Grassmann in 1844. White can be regarded as the first one who introduced the GCA in the fields of robotics [34]. The GCA is applied as a calculus for linear varieties at the symbolic level. The rows of the Jacobian matrix of a parallel mechanism can be expressed as the six screws that correspond to the Plücker coordinate vectors of six projective lines. The singular configuration of the Jacobian matrix corresponds to the configuration in which six lines become linearly dependent. Since the six screws correspond to the overall wrench system of the parallel mechanism, the target is to calculate the rank of the overall wrench system. Join "$\vee$" and meet "$\wedge$" are two operators that correspond to the span and intersection of vector spaces, respectively, defined in GCA. The super join of the above six lines corresponds to the determinant of the Jacobin matrix, which means the superbracket in GCA. The singularity of the parallel mechanism occurs when the superbracket of the overall wrench system vanishes. The superbracket is a determinant expression involving 12 points selected from six lines. The simplification is demonstrated in [30] and [35]. Through GCA, we can obtain coordinate-free algebraic expressions for the singularity conditions of parallel mechanism. More details can be found in reference [34].

To solve the singularity through GCA, first we calculate the symbolic expressions of the overall wrench system of the 2-DoF origami transmission mechanism. The second step is to calculate the superbracket of these six lines and simplify the expression. Finally, executing the decomposition of the superbracket of the overall wrench system to solve the possible conditions that lead to the vanishing of the expression. We combine the GCA results with the geometry meaning of the liner variety to identify the singular configurations of the parallel mechanism.

Three challenges we addressed in the above process can be summarized as. 1) Constructing the superbracket expression of the novel transmission mechanism. 2) Calculating the singularity condition of the superbracket. 3) Connecting the GCA statements with the geometry of the transmission mechanism configurations.

A. Constraint Wrench System

The first step is to obtain the overall wrench system of the 2-DoF origami transmission mechanism, which is the union of the constraint wrench system and the actuation wrench system. We start with calculating the constraint system. As mentioned in Section II-B, the 2-DoF origami transmission mechanism of the S^2worm has three limbs, an exoskeleton limb and two muscle limbs. The exoskeleton limb applies four constraint wrenches, which are four screws reciprocal to the twist system of the exoskeleton limb $\mathbb{S}_1$. They could be written as

$$\begin{aligned}
\mathrm{S}_{11}^r &= (\boldsymbol{e_1}; \boldsymbol{r_{A_1}} \times \boldsymbol{e_1}) \\
\mathrm{S}_{12}^r &= (\boldsymbol{e_2}; \boldsymbol{r_{A_1}} \times \boldsymbol{e_2}) \\
\mathrm{S}_{13}^r &= (\boldsymbol{e_3}; \boldsymbol{r_{A_1}} \times \boldsymbol{e_3}) \\
\mathrm{S}_{14}^r &= (0; \boldsymbol{e_1} \times \boldsymbol{e_2}).
\end{aligned} \tag{6}$$

The constraint wrenches of two muscle limbs are calculated following the same process, which is a pure moment:

$$\mathrm{S}_{21}^r = \mathrm{S}_{31}^r = (0; \boldsymbol{e_1} \times \boldsymbol{e_2}). \tag{7}$$

Thus, the constraint wrench system $\mathbb{S}_c$ of the moving platform is the union of all constraint wrench systems applied from the limbs. Since $\mathrm{S}_{21}^r = \mathrm{S}_{31}^r = \mathrm{S}_{14}^r$, $\mathbb{S}_c$ is given by

$$\mathbb{S}_c = \begin{Bmatrix} \mathrm{S}_{c1} = (\boldsymbol{e_1}; \boldsymbol{r_{A_1}} \times \boldsymbol{e_1}) \\ \mathrm{S}_{c2} = (\boldsymbol{e_2}; \boldsymbol{r_{A_1}} \times \boldsymbol{e_2}) \\ \mathrm{S}_{c3} = (\boldsymbol{e_3}; \boldsymbol{r_{A_1}} \times \boldsymbol{e_3}) \\ \mathrm{S}_{c4} = (0; \boldsymbol{e_1} \times \boldsymbol{e_2}) \end{Bmatrix}. \tag{8}$$

B. Actuation Wrench System

The actuation wrench system contains all actuation wrenches from all limbs. In a limb, by blocking the actuation joint, the actuation wrench appears reciprocal to the limb's other twists and the constraint wrenches. The actuation joints of the muscle limbs are selected as the first revolute joint corresponding to the twists. The actuation wrenches of the muscle limbs are calculated as

$$\begin{aligned}
\mathrm{S}_{a1} &= (\boldsymbol{s_2}; \boldsymbol{r_{C_2}} \times \boldsymbol{s_2}) \\
\mathrm{S}_{a2} &= (\boldsymbol{s_3}; \boldsymbol{r_{C_3}} \times \boldsymbol{s_3})
\end{aligned} \tag{9}$$

where $\boldsymbol{s_2}$ and $\boldsymbol{s_3}$ are two direction vectors defined as

$$\begin{aligned}
\boldsymbol{s_2} &= (\boldsymbol{e_1} \times (\boldsymbol{s_3} - \boldsymbol{r_{B_2}})) \times (\boldsymbol{e_2} \times (\boldsymbol{r_{D_2}} - \boldsymbol{r_{C_2}})) \\
&= (\boldsymbol{e_1} \times \boldsymbol{p_2}) \times (\boldsymbol{e_2} \times \boldsymbol{v_2}) \\
\boldsymbol{s_3} &= (\boldsymbol{e_1} \times (\boldsymbol{r_{C_3}} - \boldsymbol{r_{B_3}})) \times (\boldsymbol{e_2} \times (\boldsymbol{r_{D_3}} - \boldsymbol{r_{C_3}})) \\
&= (\boldsymbol{e_1} \times \boldsymbol{p_3}) \times (\boldsymbol{e_2} \times \boldsymbol{v_3})
\end{aligned} \tag{10}$$

where $\boldsymbol{p_2}, \boldsymbol{v_2}, \boldsymbol{p_2}, \boldsymbol{v_3}$ are direction vectors illustrated in Fig. 2. Vector $\boldsymbol{s_2}$ and $\boldsymbol{s_3}$ are the direction vectors of the intersection lines of the planes $\mathscr{P}_2$, $\mathscr{V}_2$ and planes $\mathscr{P}_3$, $\mathscr{V}_3$, respectively. Since actuation wrenches $\boldsymbol{s_2}$ and $\boldsymbol{s_3}$ also pass the points C_2 and C_3, the geometry of the wrenches are the intersection lines of the planes $\mathscr{P}_i$ and $\mathscr{V}_i (i = 2, 3)$.

C. Overall Wrench System

The overall wrench system is the union of the constraint wrench system $\mathbb{S}_c$ and the actuation wrench $\mathbb{S}_a$. The overall wrench system of the 2-DoF origami transmission mechanism is given by

$$\mathrm{W} = \mathrm{span}(\mathrm{S}_{c1}, \mathrm{S}_{c2}, \mathrm{S}_{c3}, \mathrm{S}_{c4}, \mathrm{S}_{a1}, \mathrm{S}_{a2}). \tag{11}$$

The rows of the Jacobian matrix can be expressed as the above overall wrench system in Plücker coordinate form. The singular conditions of the Jacobian matrix correspond to configurations in which the six projective lines become linearly dependent and the rank of the overall wrench system W is less than six.

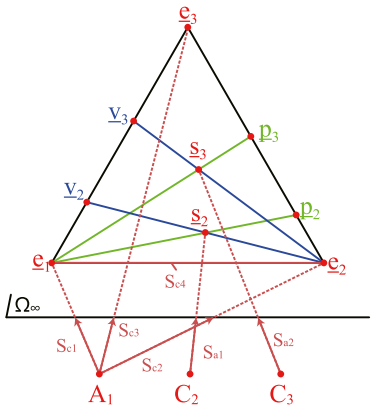

Fig. 5. Wrench graph of the 2-DoF origami transmission mechanism.

TABLE II
PROJECTIVE POINTS OF THE SCREWS

Screw	Line Type	1st Projective Point	2nd Projective point
S_{c1}	Finite	A_1	$\underline{e}_1$
S_{c2}	Finite	A_1	$\underline{e}_2$
S_{c3}	Finite	A_1	$\underline{e}_3$
S_{c4}	Infinite	$\underline{e}_1$	$\underline{e}_2$
S_{a1}	Finite	C_2	$\underline{s}_2$
S_{a2}	Finite	C_3	$\underline{s}_3$

D. Superbracket of the 2-DoF Origami Transmission Mechanism

The overall wrench system of the 2-DoF origami transmission mechanism is obtained in (11). To solve all the singular conditions of the mechanism through GCA, we need to find two points for each screw to calculate the superbracket of the mechanism.

Screws represent lines in projective space and can be classified as infinite lines and finite lines. Infinite lines only contain infinite points. Finite lines must include at least one finite point, the other point can be either finite or infinite. The direction vector corresponds to a point at infinity. In the following analysis, the infinite points are denoted with an underline to differentiate them from the finite points. S_{c1}, S_{c2}, and S_{c3} are finite lines which all pass point A_1. The second infinite points of the above three wrenches are chosen as $\underline{e}_1$, $\underline{e}_2$, and $\underline{e}_3$ respectively. S_{c4} is an infinite line and the two points are chosen as $\underline{e}_1$ and $\underline{e}_2$.

The point on the actuation wrench S_{a1} are chosen as $\underline{s}_2$ and C_2. In the projective space, follow the (10), point $\underline{s}_2$ is the intersection of projective line $\underline{e}_1\underline{p}_2$ and $\underline{e}_2\underline{v}_2$. Since vector $\boldsymbol{p_2}$ is orthogonal to vector $\boldsymbol{e_1}$, thus projective point $\underline{p}_2$ belongs to projective line $\underline{e}_2\underline{e}_3$. Vector $\boldsymbol{v_2}$ is orthogonal to vector $\boldsymbol{e_2}$, thus projective point $\underline{v}_2$ belongs to projective line $\underline{e}_1\underline{e}_3$. Similarly, the projective points on the actuation wrench S_{a2} is chosen as $\underline{s}_2$ and C_3. Projective point $\underline{s}_3$ is the intersection of the projective line $\underline{e}_1\underline{p}_3$ and $\underline{e}_2\underline{v}_3$. While $\underline{p}_3$ belongs to projective line $\underline{e}_2\underline{e}_3$ and $\underline{v}_3$ belongs to projective line $\underline{e}_1\underline{e}_3$.

Following the above analysis, we can draw the wrench graph in the projective space (see Fig. 5). Screws and points are listed in Table II. All 12 projective points from the overall wrench system are obtained as: $S_{c1} = A_1\underline{e}_1$, $S_{c2} = A_1\underline{e}_2$, $S_{c3} = A_1\underline{e}_3$, $S_{c4} = \underline{e}_1\underline{e}_2$, $S_{a1} = C_2\underline{s}_2$ and $S_{a2} = C_3\underline{s}_3$. The superbracket of the 2-DoF origami transmission mechanism is

$$\text{Superbracket} = [A_1\underline{e}_1, A_1\underline{e}_2, A_1\underline{e}_3, C_2\underline{s}_2, \underline{e}_1\underline{e}_2, C_3\underline{s}_3]. \quad (12)$$

E. Superbracket Decomposition

Following the superbracket calculation and simplification method [30], [35], (12) can be expended and simplified as:

$$\begin{aligned}&\text{Superbracket}\\ &= [A_1\underline{e}_1\underline{e}_2\underline{e}_3][A_1C_2\underline{s}_2\underline{e}_2][A_1\underline{e}_1C_3\underline{s}_3]\\ &\quad - [A_1\underline{e}_1\underline{e}_2\underline{e}_3][A_1C_2\underline{s}_2\underline{e}_1][A_1\underline{e}_2C_3\underline{s}_3]\\ &= [A_1\underline{e}_1\underline{e}_2\underline{e}_3][A_1C_2\underline{s}_2\dot{\underline{e}}_2][A_1\dot{\underline{e}}_1C_3\underline{s}_3] \quad (13)\end{aligned}$$

where the dotted letters ■ stand for permuted elements as explained in [30].

The singularity happens when (13) equals zero. The superbracket is decomposed and discussed as follows.

a) The first term $[A_1\underline{e}_1\underline{e}_2\underline{e}_3]$ is equal to zero. The corresponding geometry condition is that points A_1, $\underline{e}_1$, $\underline{e}_2$, $\underline{e}_3$ are coplanar. This condition is impossible since A_1 is a finite point and $\underline{e}_1$, $\underline{e}_2$, $\underline{e}_3$ are three infinite points, which correspond to three orthogonal directions vectors.

b) The second term $[A_1C_2\underline{s}_2\dot{\underline{e}}_2][A_1\dot{\underline{e}}_1C_3\underline{s}_3]$ is equal to zero. This bracket statement corresponds to the GCA statement

$$(A_1C_2\underline{s}_2) \wedge (A_1C_3\underline{s}_3) \wedge (\underline{e}_1\underline{e}_2) = 0. \quad (14)$$

Equation. (14) occurs when one of the following conditions is verified.

b.1) $(\underline{e}_1\underline{e}_2) = 0 \Rightarrow$ line $(\underline{e}_1\underline{e}_2)$ degenerates. This condition is impossible.

b.2) $(A_1C_2\underline{s}_2) = 0 \Rightarrow$ plane $(A_1C_2\underline{s}_2)$ degenerates, projective points A_1, C_2, $\underline{s}_2$ are aligned. Actuation wrench S_{a1} passes point A_1. This corresponds to the structure configuration that planes $\mathscr{P}_2$ and $\mathscr{V}_2$ pass the point A_1.

b.3) $(A_1C_3\underline{s}_3) = 0 \Rightarrow$ plane $(A_1C_3\underline{s}_3)$ degenerates, projective points A_1, C_3, $\underline{s}_3$ are aligned. Actuation wrench S_{a2} passes point A_1. This corresponds to the structure configuration that planes $\mathscr{P}_3$ and $\mathscr{V}_3$ pass the point A_1.

b.4) $(A_1C_2\underline{s}_2) \wedge (\underline{e}_1\underline{e}_2) = 0 \Rightarrow$ Points A_1, C_2, $\underline{s}_2$, $\underline{e}_1$, $\underline{e}_2$ coplanar, actuation wrench S_{a1} lies in the plane $(A_1\underline{e}_1\underline{e}_2)$. This condition can be satisfied when planes $\mathscr{V}_2$ and $\mathscr{M}$ coincide.

b.5) $(A_1C_3\underline{s}_3) \wedge (\underline{e}_1\underline{e}_2) = 0 \Rightarrow$ Points A_1, C_3, $\underline{s}_3$, $\underline{e}_1$, $\underline{e}_2$ coplanar, actuation wrench S_{a2} lies in the plane $(A_1\underline{e}_1\underline{e}_2)$. This condition can be satisfied when planes $\mathscr{V}_3$ and $\mathscr{M}$ coincide.

b.6) $(A_1C_2\underline{s}_2) \wedge (A_1C_3\underline{s}_3) = 0 \Rightarrow$Points $A_1, C_2, \underline{s}_2, C_3$, $\underline{s}_3$, coplanar, actuation wrenches S_{a1} and S_{a2} span a

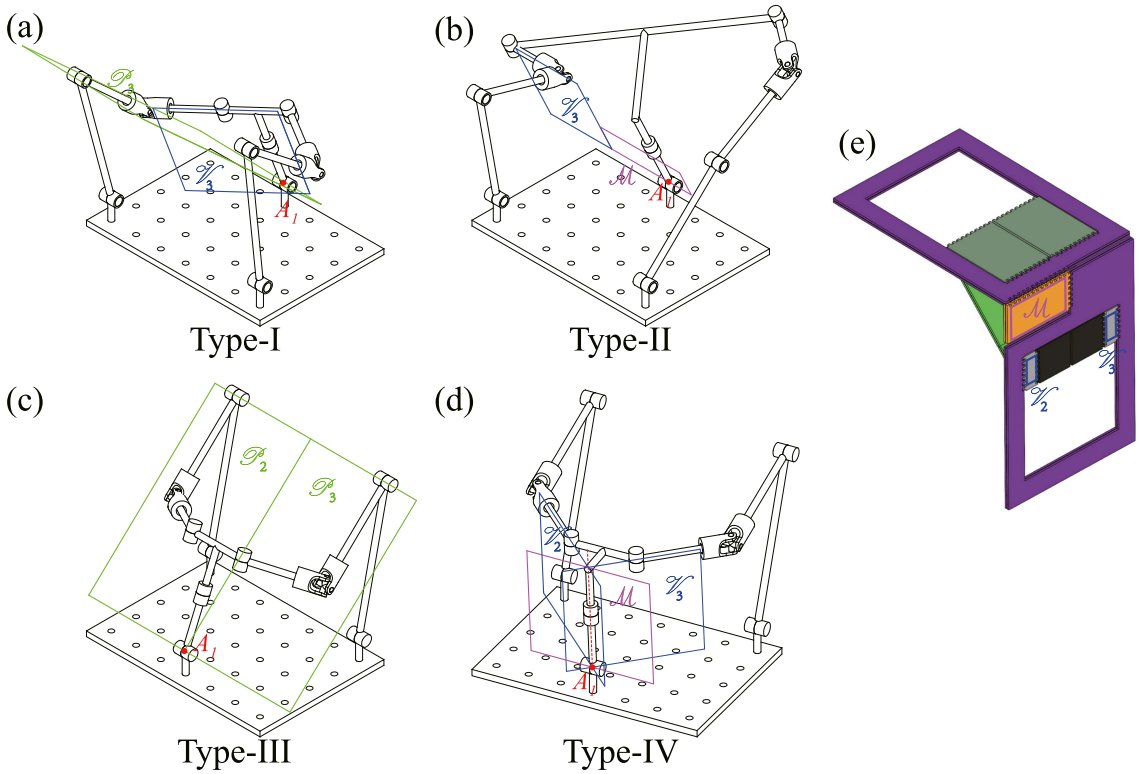

Fig. 6. (a)–(d) Four types of singular configurations. (a) *Type-I*, plane $\mathscr{P}_3$ and $\mathscr{V}_3$ both pass the point A_1. (b) *Type-II*, Plane $\mathscr{V}_3$ and $\mathscr{M}$ are coplanar. (c) *Type-III*, Plane $\mathscr{P}_2$ and $\mathscr{P}_3$ are coplanar and both pass the point A_1. (d) *Type-IV*, Plane $\mathscr{V}_2$ $\mathscr{V}_3$ and $\mathscr{M}$ have a common intersection line which pass the point A_1. (e) The initial configuration of the SCM structure in the previous S^{2}worm [19]. Planes $\mathscr{V}_2$, $\mathscr{V}_3$, and $\mathscr{M}$ are coplanar. This geometry meets the conditions of *Type-II* and *Type-IV*.

plan which passes the point A_1. This condition can be satisfied when planes $\mathscr{P}_2$ and $\mathscr{P}_3$ coincide and both pass the point A_1.

b.7) $(\mathrm{A_1C_2\underline{s}_2}) \wedge (\mathrm{A_1C_3\underline{s}_3}) \wedge (\underline{\mathrm{e}}_1\underline{\mathrm{e}}_2) = 0 \Rightarrow$ the intersection line of the planes $(\mathrm{A_1C_2\underline{s}_2})$ and $(\mathrm{A_1C_3\underline{s}_3})$ coplanar with the line $(\underline{\mathrm{e}}_1\underline{\mathrm{e}}_2)$. This condition can be satisfied when planes $\mathscr{V}_2$, $\mathscr{V}_3$ and $\mathscr{M}$ have a common intersection line.

Thus, we present the exhaustive singularity analysis of the 2-DoF origami transmission mechanism. All singular conditions of the mechanism are listed and can be classified into four types:

1) *Type-I*: (b.2) and (b.3), one of the actuation wrenches passes the point A_1.
2) *Type-II*: (b.4) and (b.5), one of the actuation wrenches lies in the plane $(\mathrm{A_1}\underline{\mathrm{e}}_1\underline{\mathrm{e}}_2)$.
3) *Type-III*: (b.6), the plane spanned by two actuation wrenches passes the point A_1.
4) *Type-IV:* (b.7), the intersection line of the plane $(\mathrm{A_1C_2\underline{s}_2})$ and $(\mathrm{A_1C_3\underline{s}_3})$ belongs to the plane $(\mathrm{A_1}\underline{\mathrm{e}}_1\underline{\mathrm{e}}_2)$.

We have obtained all the possible singular configurations of the 2-DoF origami transmission mechanism through the GCA and the results are illustrated in Fig. 6. As mentioned before, GG and GCA are two approaches that are complementary to each other in geometry and algebra aspects, respectively. Here, we list the correspondence between the four types of singular conditions and the classification of linear varieties of GG in Table III.

Based on the above analysis, we recall the SCM design of the S^{2}worm in our previous work. At the initial configuration [see Fig. 6(e)], two actuation wrenches lie in the plane $(\mathrm{A_1}\underline{\mathrm{e}}_1\underline{\mathrm{e}}_2)$. This geometry corresponds to the *Type-II*, *Type-III*, and *Type-IV* singular conditions, which cause the low actuation efficiency of the driving system at the initial configuration and the following turning motion. The solution is to make the actuation wrenches as perpendicular to the plane $(\mathrm{A_1}\underline{\mathrm{e}}_1\underline{\mathrm{e}}_2)$ as possible, the solution will be fully explained with the SCM design in Section IV-A.

By applying GCA, we can calculate all the possible singularities of the SCM structure. The singularity of the previous design can be explained. Moreover, we can refine the SCM structure to avoid the singularity.

F. Justification of the Singularity Analysis

So far, all the singularity analyses are based on the rigid body system assumption, while the SCM structure is connected through soft PI membrane joints. Here, we make a justification that the SCM structure can be treated as a rigid body system during the singularity analysis since the stiffness of the soft joint does not affect the results.

In the aspect of compliant mechanism [36], a living hinge is defined as extremely short and thin small-length flexural pivots. In the SCM structure, the soft joint consistent with this definition for the castle-like edges is extremely close. The distance is only $\sim 25\mu$m caused by the laser ablation. Following the definition of the living hinge, the soft joint can be considered a torsion spring with low rigidity. These soft joints applied small torques to the SCM structure.

TABLE III
SINGULAR CONDITIONS OF THE 2-DOF ORIGAMI TRANSMISSION MECHANISM: CORRESPONDENCE BETWEEN GCA AND GG

Singularity Type	GCA Statement	Structure Configuration
Type-I	$(\mathrm{A_1C_2\underline{S}_2}) = 0$ or $(\mathrm{A_1C_3\underline{S}_3}) = 0$	Plane $\mathscr{P}_2$ and $\mathscr{V}_2$ (or $\mathscr{P}_3$ and $\mathscr{V}_3$) both pass the point A_1.
Type-II	$(\mathrm{A_1C_2\underline{S}_2}) \wedge (\underline{\mathrm{e}}_1\underline{\mathrm{e}}_2) = 0$ or $(\mathrm{A_1C_3\underline{S}_3}) \wedge (\underline{\mathrm{e}}_1\underline{\mathrm{e}}_2) = 0$	Plane $\mathscr{V}_2$ (or $\mathscr{V}_3$) and $\mathscr{M}$ are coplanar.
Type-III	$(\mathrm{A_1C_2\underline{S}_2}) \wedge (\mathrm{A_1C_3\underline{S}_3}) = 0$	Plane $\mathscr{P}_2$ and $\mathscr{P}_3$ are coplanar and both pass the point A_1.
Type-IV	$(\mathrm{A_1C_2\underline{S}_2}) \wedge (\mathrm{A_1C_3\underline{S}_3}) \wedge (\underline{\mathrm{e}}_1\underline{\mathrm{e}}_2) = 0$	Plane $\mathscr{V}_2$ $\mathscr{V}_3$ and $\mathscr{M}$ have a common intersection line which pass the point A_1.

Singularity Type	Linear Variety Geometry	GG Classification [29]
Type-I	S_{a1} (or S_{a2}) S_{c1} S_{c2} S_{c3}coucur	3c. All lines through a point
Type-II	S_{a1} (or S_{a2}) S_{c1} S_{c2} S_{c4} are coplanar	3d. All lines in plane
Type-III	S_{a1} S_{a2} span a plane passes the point A_1, S_{c1} S_{c2} S_{c3} pass the point A_1	4d. Degenerate congruence. All the lines in plane or pass the point in that plane
Type-IV	The planes which contain S_{a1} S_{a2} S_{c1} S_{c2} S_{c3} intersect at a common line	4c. Parabolic congruence.A one parameter family of flat pencils, having one line in common and forming a variety.

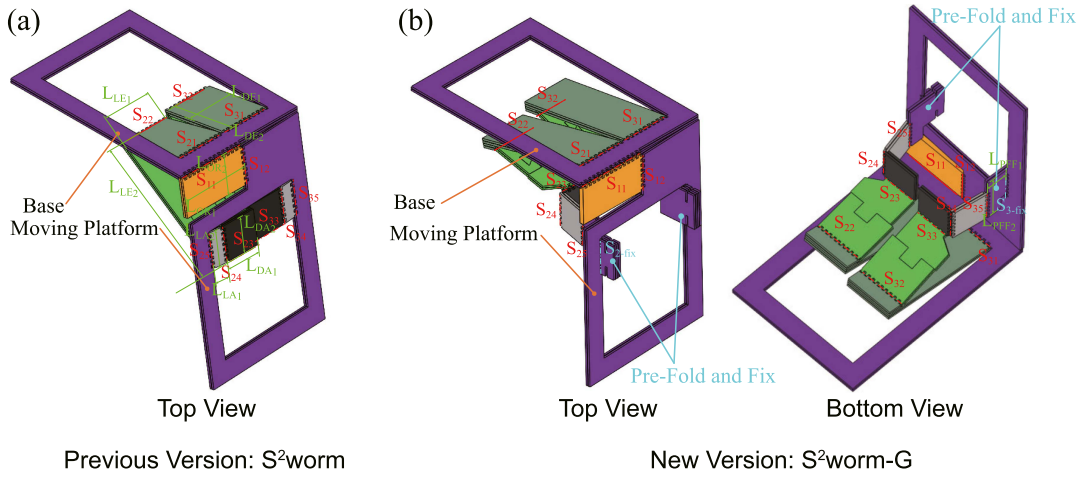

Fig. 7. SCM structure of the 2-DoF origami transmission of the (a) S²worm and (b) S²worm-G. Sideboards and slider-crank mechanisms are hidden for easy understanding.

Since these torques are parallel to the joint axis, these torques act at the limb twist subspace [see (1) and (2)]. This subspace is reciprocal to the limb constraint wrench subspace [see (8)], which means it will not affect the constraint wrench system provided by the limbs. An exception is the torque generated by the PI membrane at the actuation joints will be superimposed with the actuation torque, which will influence the magnitude of the actuation wrench system [see (9)] but will not affect the direction of the actuation wrenches. The form of the actuation wrenches is also reserved. The singularity analysis of the system considers the joint stiffness will lead to the same singular configuration as the corresponding rigid body architecture. Thus, the SCM structure can be treated as a rigid body system during the singularity analysis as long as it meets the living hinge definition.

IV. DESIGN AND FABRICATION

A. Improvement of 2-DoF Origami Transmission Mechanism

In this section, we further refine the SCM design to promote the actuation effect. Based on the geometry notation of the 2-DoF origami transmission mechanism, the planes we define correspond to the specific links of the SCM structure. Fig. 7 shows the geometry of the 2-DoF origami transmission mechanism between the previous version and the current version. All links are referred to via their color. The planes $\mathscr{P}_i (i = 2, 3)$ (see Fig. 2) corresponds to the light green links between the twists S_{i2} and $\mathrm{S}_{i3} (i = 2, 3)$. The planes $\mathscr{V}_i (i = 2, 3)$ corresponds to the gray links between the twists S_{i4} and $\mathrm{S}_{i5} (i = 2, 3)$. The planes $\mathscr{M}$ corresponds to the orange link between the twists S_{11} and S_{12}.

In the SCM structure, the most common condition that may lead to singularity is that several links become coplanar. Because SCM is a two-dimension fabrication method and structures are folded to complete. In the 2-DoF origami transmission mechanism of the S²worm-G, *Type-I* singular condition occurs seldom since it is difficult to satisfy both planes $\mathscr{P}_i$ and $\mathscr{V}_i$ pass the point A_1, which refers to the light green links and the gray links both pass the point A_1. Generally, this condition is hardly satisfied in the SCM design since the light green links need to fold to achieve the close loop in our design.

TABLE IV
COMPARISON OF THE GEOMETRY PARAMETERS OF THE 2-DOF ORIGAMI TRANSMISSION MECHANISM BETWEEN S^2 WORM AND S^2 WORM-G

Link	Corresponding Twists	Notation in Fig. 7	S^2worm (mm)	S^2worm-G (mm)
Dark Green	S_{i1} and S_{i2} $i = 2, 3$	L_{DE_1} L_{DE_2}	5 7	4.8 10.8
Light Green	S_{i2} and S_{i3} $i = 2, 3$	L_{LE_1} L_{LE_2}	5 13	4.8 7
Dark Gray	S_{i3} and S_{i4} $i = 2, 3$	L_{DA_1} L_{DA_2}	3.6 3.4	3.6 3.4
Light Gray	S_{i4} and S_{i5} $i = 2, 3$	L_{LA_1} L_{LA_2}	1.5 3.4	3.5 3.4
Orange	S_{i4} and S_{i5} $i = 2, 3$	L_{Or_1} L_{Or_2}	7 3.75	7 3.75
Pre-Fold and Fix	S_{i5} and S_{i-fix} $i = 2, 3$	L_{PFF_1} L_{PFF_2}	— —	2.1 4.9

At the initial configuration (see Fig. 6), the gray links and the orange link are coplanar. Two actuation wrenches S_{a1} and S_{a2} both lie in the plane $(A_1\underline{e}_1\underline{e}_2)$, this geometry leads to the singular condition *Type-II*, *Type-III,* and *Type-IV*. To avoid the singularities of the robot, *the method is to avoid the gray links and the orange link to be coplanar*. Moreover, to maximize the actuation effect, we tend to make the actuation wrenches as perpendicular to the projective plane $(A_1\underline{e}_1\underline{e}_2)$ as possible. Since the actuation wrenches S_{a1} and S_{a2} are the intersection lines of the light green links and the gray links, and the plane $(A_1\underline{e}_1\underline{e}_2)$ corresponds to the orange link. In this work, to refine the SCM structure, *the only simple correction* is to make the gray links as perpendicular to the orange link as possible at the initial configuration.

In the new version of the SCM structure, we apply a method named "Pre-Fold and Fix" to maintain the gray links perpendicular to the orange link. The specific method is to add two additional links between the gray links and the moving platform. The "Pre-Fold and Fix" links and the moving platform are connected with the joints S_{2-fix} and S_{3-fix}. These two links are folded perpendicular to the moving platform and fixed. Recall the limitation of the SCM method that a joint can hardly rotate over 90°, adding the "Pre-Fold and Fix" links in the S^2worm-G allows the twists $S_{i5}(i = 2, 3)$ to rotate freely, since the initial configuration of the gray links and "Pre-Fold and Fix" links are nearly coplanar [otherwise the gray links connect to the moving platform directly will lead to the twist $S_{i5}(i = 2, 3)$ rotate nearly or over 90°]. Besides, the lengths of the other links of the SCM structure are slightly changed to fit this change. All the design parameters are listed in Table IV.

B. Evaluation of the Improvement

LSI is applied to mathematically evaluate the improvement of the refined transmission mechanism. The LSI has a range of [0, 1], a large value indicates a larger "distance" from the current configuration to the singular configuration. Singular configuration corresponds to LSI $= 0$.

The LSI values of the previous and the new versions of the origami transmission mechanism are calculated. The distribution of the values is presented in Fig. 9. During the calculation, the range of the lift and twist motion are both selected as $[-10, 10]^\circ$.

It is shown that the previous mechanism has a singularity problem, the range of the LSI value is $[0, 0.193]$. The refined transmission mechanism has a large LSI range of $[0.349, 0.515]$, which implies the transmission efficacy is significantly improved.

C. Transmission Mechanism and Actuator

According to the SCM fabrication principle, the compliant linkage is achieved by a flexible sheet sandwiched by two rigid sheets. Generally, additional adhesive sheets are introduced for bonding. In this work, the flexible film, the rigid sheets, and the adhesive sheets are selected as Polyimide film (PI), carbon fiber (CF), and the Dupont FR1500 sheet adhesive (FR1500), respectively. The details of the materials are listed in Table V. A compliant linkage is thus formed by a five-layer stack: CF-Adhesive-PI-Adhesive-CF.

The whole SCM structure of the S^2worm-G can be separated into two slider-crank mechanisms plus the 2-DoF origami transmission mechanism. The fabrication and assembly process of the SCM structure is more complicated compared with the first generation of the S^2worm. Since we refine the 2-DoF origami transmission mechanism by enlarging the length of the gray linksL_{LA_1}, the two gray links, two black links, and the purple link (see Fig. 7) can no longer be tiled in a single five-layer stack.

To solve this problem, an additional five-layer stack is introduced. The fabrication process of the SCM structure starts with three five-layer stacks [see Fig. 8(a)]. The top stack is for the slider-crank mechanism. The middle and bottom stacks construct the 2-DoF origami transmission mechanism together. The three stacks are cured and then laser cut into three laminates separately. After that, two adhesive sheets are introduced between these two laminates to bond. The stack above is then cured and cut out of the frame for folding and assembly. The light green bars are reconnected to construct the close loop structure [19], [24]. The gray links are folded vertically to the

TABLE V
MATERIALS OF THE TRANSMISSION MECHANISM AND THE ACTUATOR

Component	Material	Abbreviation in Fig. 8	Thickness (μm)
Transmission Mechanism	Carbon Fiber	CF	200
	Dupont FR1500 Sheet Adhesive	Adhesive	12.5
	Polyimide Film	PI	12.5
Actuator	Epoxy Glass Cloth	FR4	127
	Piezoelectric Ceramic	PZT	127
	Alumina Ceramic	Al	127
	Unidirectional Carbon Fiber Prepreg	Uni-CF	50
	Bidirectional Carbon Fiber Prepreg	Bi-CF	200
	Copper Foil	Cu	13

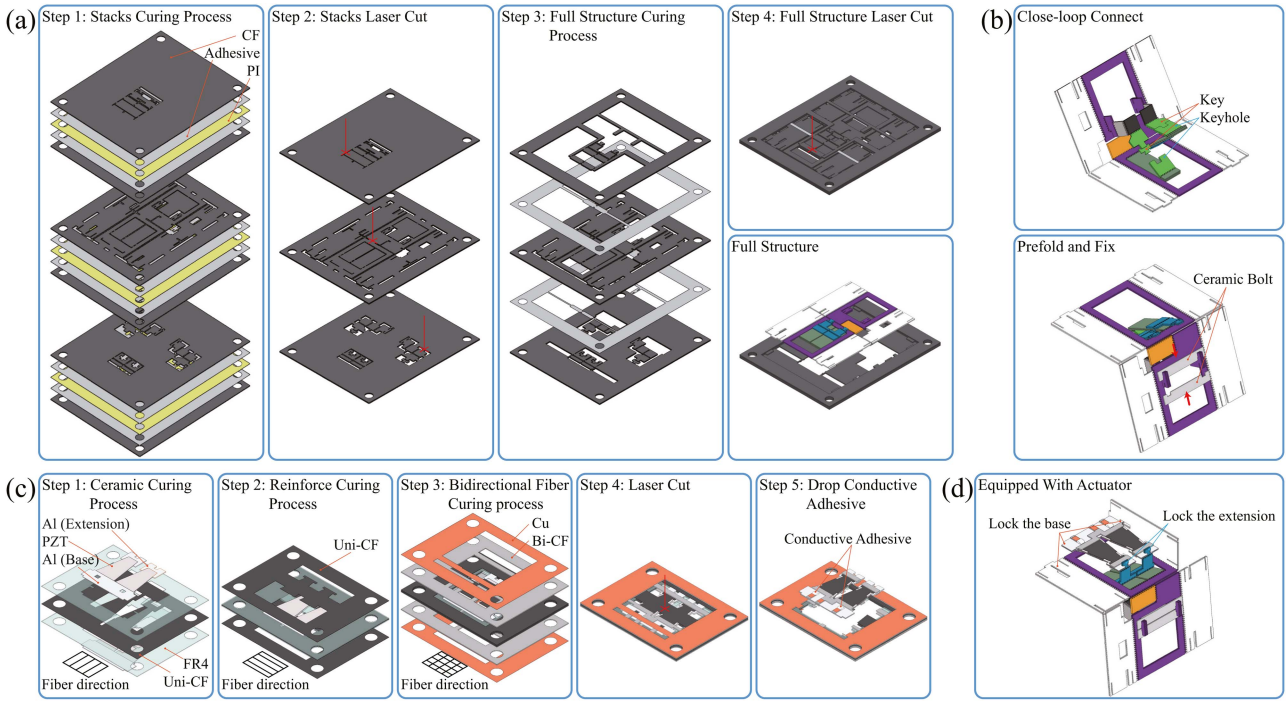

Fig. 8. (a) Fabrication process of the transmission mechanism. (b) Connect and fix of the transmission mechanism. (c) Fabrication process of the double deck piezoelectric actuator. (d) Assembly process of the actuator.

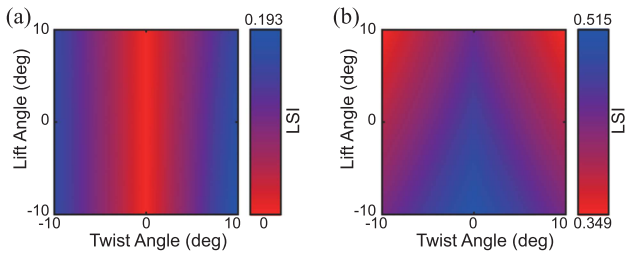

Fig. 9. LSI distribution of origami transmission mechanism. (a) S^2worm. (b) S^2worm-G.

moving platform and two 200 μm alumina ceramic bolts are plugged to fix the gray links. As mentioned before, this can maintain the gray links perpendicular to the orange link at the initial configuration, which can make the 2-DoF origami transmission mechanism avoid the singular condition and promote the actuation effect. The above processes are presented in Fig. 8(b). Thus, the SCM structure is prepared for equipping the actuator.

The fabrication process of the double deck piezoelectric actuator can be separated into five steps [see Fig. 8(c)] and the material properties are listed in Table V. First, the unidirectional carbon fiber prepreg is sandwiched by the ceramics aligned in a FR4 frame and then cured into a three-layer stack. At this step, both the top and bottom ceramic layers contain five pieces of ceramics. Among these ceramics, two of them are trapezoid PZTs, two of them are alumina ceramics named extension, and one of them is alumina ceramics named base. It needs to be mentioned that the fiber direction is parallel to the height direction of the trapezoidal PZTs. In the second step, the stack is sandwiched by two unidirectional carbon fiber prepregs and then cured into a five-layer stack. At this step, the fiber direction is parallel to the bottom edge of the trapezoidal PZTs. The horizontal unidirectional carbon fiber prepreg can reinforce the PZTs. During the third step, the five-layer stack is sandwiched

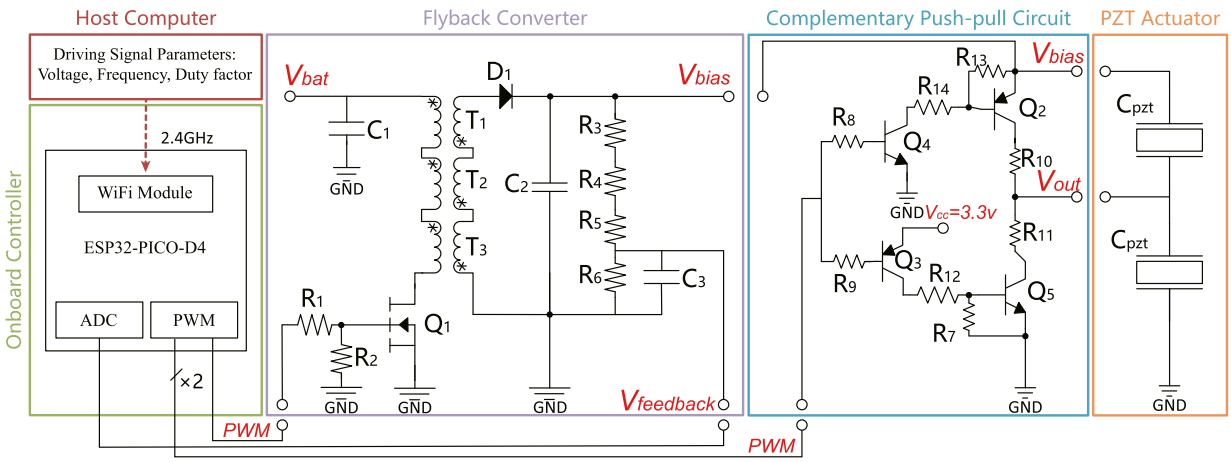

Fig. 10. Circuit Schematic of the onboard electronics. The onboard controller communicates with the host computer through the WiFi module to receive the control commands. The high voltage boost converter can be separated into a flyback converter circuit for generating a high level voltage (V_{bias}) and two complementary push–pull circuits for generating square wave high voltage (V_{out}).

by two bidirectional carbon fiber prepreg and two copper sheets. The bidirectional carbon fiber bridge is the interface between the PZT ceramic and the alumina ceramic. This step can also create electric contacts. During the fourth step, the actuator is cut out of the FR4 frame by laser. Finally, the conductive adhesive is dropped to fill the hole on the alumina ceramic base to connect the middle layer unidirectional carbon fiber prepreg and the top layer copper electrode.

The process of equipping the SCM structure with the actuator is illustrated in Fig. 8(d). First, the base of the actuator is inserted into the holes on the side boards of the SCM structure and glued. Then, the slider-crank mechanisms of the SCM structure are connected to the extensions of the actuator individually.

D. Onboard Electronics

To achieve the untethered locomotion of the insect-scale robot, we equipped the S^{2}worm-G robot with the onboard power source and electronics. In this work, a 3.7 V 35 mAh rechargeable lithium battery is chosen as the power source. The onboard electronics include the customized high voltage boost converter for driving the PZTs and the onboard controller for receiving the commands and generating the control signals (see Fig. 10). The components of the electronic circuit are listed in Table VI.

The electronics are mainly adopted from the previous work [19]. The onboard controller communicates with the host computer through the Wi-Fi module to receive the control commands. The high voltage boost converter can be separated into a flyback converter circuit for generating a high level voltage (V_{bias}) and two complementary push–pull circuits for generating square wave high voltage (V_{out}). The circuit of the piezoelectric actuator is simultaneous configuration [37]. A single deck can be considered as two PZT capacitors in series. The top PZT capacitor is under the voltage $V_{\text{top}} = V_{\text{bias}} - V_{\text{out}}$, and the bottom PZT capacitor is under the voltage $V_{\text{bottom}} = V_{\text{out}} - V_{\text{GND}} = V_{\text{out}}$. The resultant driving signal of a single PZT deck is calculated as

$$V_{\text{drive}} = V_{\text{top}} - V_{\text{bottom}} = V_{\text{bias}} - 2V_{\text{out}}. \tag{15}$$

TABLE VI
COMPONENTS OF THE ONBOARD ELECTRONICS OF THE S^{2}WORM-G IN FIG. 10

Description	Notation in Fig. 10	Parameters and model
Capacitor	C_1, C_2, C_3	1 uF(0402),1 uF(2220), 1 nF(0402)
Resistor	R_1,R_2, R_3-R_5, R_6-R_7, R_8-R_{12}, R_{13}, R_{14}	200 Ω(0603), 20 kΩ(0603), 3.3 MΩ(0402),100 kΩ(0402), 10 kΩ(0402), 499 kΩ(0402), 2 MΩ(0402)
Diode	D_1	US1NWF-7
Transformer	T_1, T_2, T_3	ATB322515-0110-T000
MOSFET	Q_1	SI2324DS-T1-GE3
PNP	Q_2, Q_3	STR2550
NPN	Q_4, Q_5	STR1550

This conclusion is applied in Section V-A.

Compared with the previous circuit in [19], three modifications need to be pointed out.

1) One more transformer (T_3) is added in series to improve the load capacity of the flyback converter and reduce heat.
2) A feedback sample circuit is added in the flyback converter (R_3, R_4, R_5, R_6, C_3) for achieving the close-loop control of the high level voltage V_{bias}. The feedback signal is sent into the ADC module of the onboard controller.
3) The resistor R_{14} in the complementary push–pull circuit is reduced from 15 to 2 MΩ. This reduction can, in view of the results, make the uprising edge of the driving signal V_{drive} sharper.

The main components of the S^{2}worm-G prototype can be summarized as the SCM structure, the double deck piezoelectric actuator, the battery, and the onboard electronics. The mass distribution of the S^{2}worm-G is listed in Table VII. The new transmission mechanism brings only 0.1 g additional mass. Compared with the mass of the whole robot, this change can be neglected.

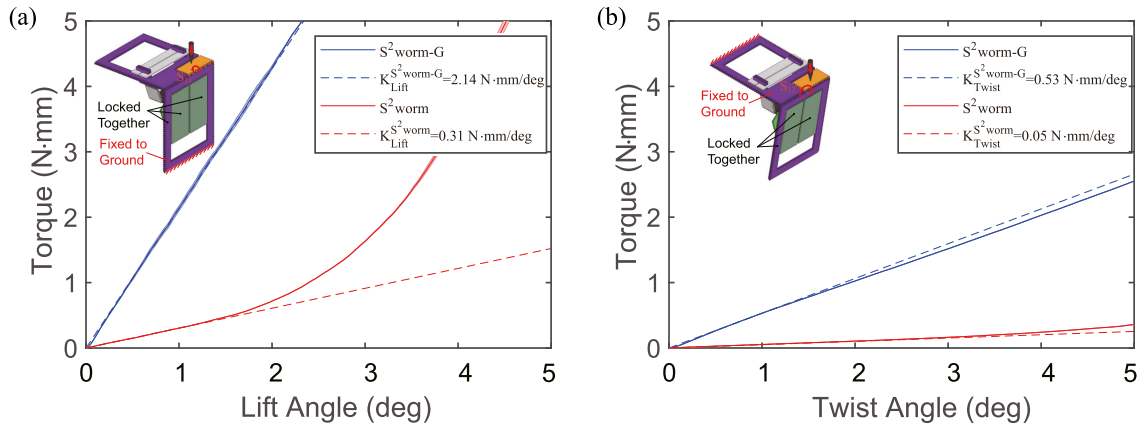

Fig. 11. (a) Stiffness test of the lift motion. The stiffness of the current version S²worm-G is 7 times higher than before. (b) Stiffness test of the twist motion. The stiffness of the current version S²worm-G is almost 10 times higher than before.

TABLE VII
MASS DISTRIBUTION OF THE S²WORM AND S²WORM-G

Component	S²worm (g)	S²worm-G (g)
Transmission Mechanism	0.80	0.81
Actuator	0.28	0.39
Battery	1.48	1.52
Onboard Electronics	1.51	1.80
Wires, Solder and Glue	0.27	0.19
Total	4.34	4.71

V. EXPERIMENTS

In this section, we mainly focus on the characterization of the SCM structure and the S²worm-G. For the refined SCM structure, we compared the stiffness between the previous and the current version to prove the singularity of the SCM structure during the lift and twist motion has been fully solved. For the S²worm-G robot, we measure the speed during the forward and turning locomotion. The speeds of several different substrates are tested to prove the surface adaptability of the robot. The energy consumption of the robot is calculated. We adopt the performance metrics proposed in [11] to compare this work with related works and insects.

A. Experimental Verification for the Singularity of the Lift and Twist Motion

To compare the structure stiffness between the old version and the current version of the 2-DoF origami transmission mechanism, we present the stiffness test on both lift and twist motion (see Supplementary Movie S4). The 2-DoF origami structure is fixed for the test. The input links and the fixed platform are locked together and the load is applied through a test needle connected to the mechanical testing system (INSTRON 5944). The base and the moving platform are fixed to the ground for loading. The displacement and force of the needle are recorded. The corresponding angles and torque are calculated for comparison (see Fig. 11).

The stiffness of the 2-DoF origami transmission mechanism can be calculated as $K = \frac{\text{Torque}}{\text{Angle}}$. In this work, the secant stiffness of the curve is calculated as $K = \frac{\text{Torque@1deg}}{\text{1deg}}$. For the previous version in the S²worm, the stiffness of the lift and twist motion are calculated as $K_{\text{Lift}}^{S^2\text{worm}} = 0.31$ N·mm/deg and $K_{\text{Twist}}^{S^2\text{worm}} = 0.05$ N·mm/deg, respectively. For the current version, after refined, the stiffness achieves $K_{\text{Lift}}^{S^2\text{worm}-G} = 2.14$ N·mm/deg for lift motion and $K_{\text{Twist}}^{S^2\text{worm}-G} = 0.53$ N·mm/deg for twist motion. The stiffness of the current version is 7 times higher for the lift motion and 10 times higher for the twist motion. It proves that the singularity of the 2-DoF origami transmission mechanism has been effectively solved through the SCM design instructed by the GCA calculation.

B. Characterization of the Actuator

The double deck piezoelectric actuator generates the deflection at the tip. The tip alumina ceramic extension is connected to the slider-crank mechanism of the SCM structure. We measure the free deflection of the actuator driven by the custom designed high voltage boost converter. The deflection of the actuator is sampled by the laser sensor (KEYENCE, LK-G10) and the voltage signals are recorded by an oscilloscope (Tektronix, MDO 34).

The free deflection and the driving signal are shown in Fig. 12. The driving signals is defined in (15) as: $V_{\text{drive}} = V_{\text{bias}} - 2V_{\text{out}}$.

The test voltages (actually the bias voltage of the high voltage boost converter) are set as 160, 180, 200, and 220 V and the frequencies range from 10 to 150 Hz. The Peak-to-Peak (PP) deflection is recorded in the Fig. 12(a).

Attributed to the feedback of the high voltage boost converter, the waveforms are more like the square wave even at the high frequency. At this condition, the maximum free deflection of the actuator does not show a downward trend at the relatively high frequency (In our previous work, limited by the load capacity of the high voltage boost converter, the distortion of the waveform leads to the decrease of the free deflection of the actuator). In this work, the limitation still exists at a higher set frequency, Fig. 12(b) shows the ripple of signals at 140 and 150 Hz, 200 and 220 V. Since the load of the high voltage boost converter is heavy, the high level of the bias signals shows instability.

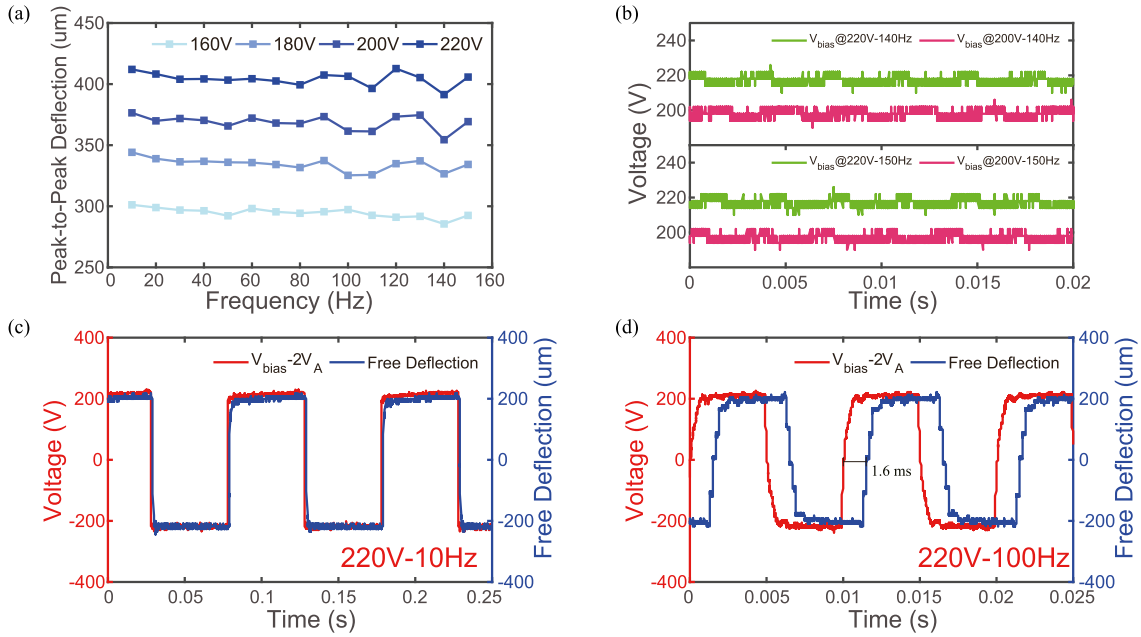

Fig. 12. (a) Free deflection of the double deck piezoelectric actuator with different driven voltages and frequencies. (b) The ripple of the bias voltages when the set values are 200 and 220 V with 140 and 150 Hz. Limited by the load capacity of the onboard electronics, the shape of the wave is not as perfect as the signal at relatively low voltage and frequency. (c) Waveforms of the voltage and tip free deflection at 220 V–10 Hz. The rising edges of the voltage and the deflection are almost simultaneously. (d) Waveforms of the voltage and tip free deflection at 220 V–100 Hz. The rising edge of the deflection is 1.6 ms slower than the rising edge of the voltage.

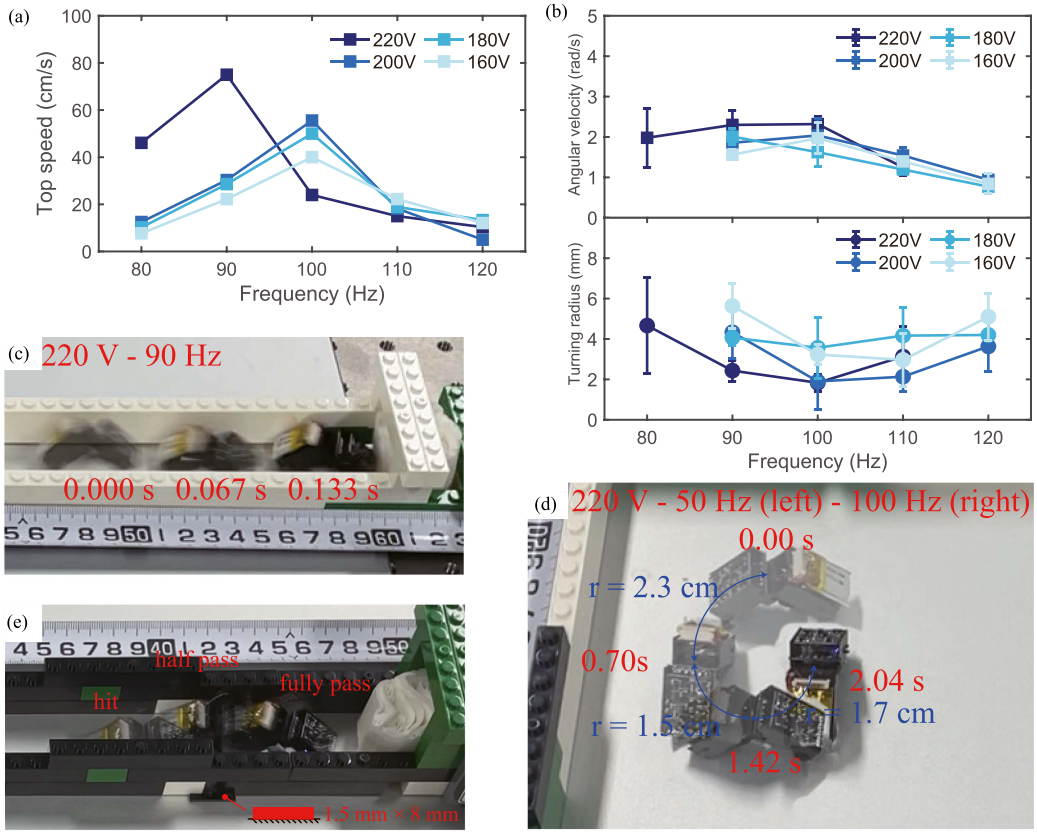

Fig. 13. (a) Speed test of the S^{2}worm-G. The top speed achieves 75.0 cm/s at 220 V–90 Hz. (b) Turning test of the S^{2}worm-G. The maximum angular velocity and the minimum turning radius both occur at 220 V–50 Hz–100 Hz. The X axis ticks are the frequency of the right deck. The frequency of the left deck is half of the right deck to allow the robot to make anti-clockwise turns. (c) Snapshots of the S^{2}worm-G at 75.0 cm/s. (d) Snapshots of the S^{2}worm-G turning at average angular velocity 2.32 rad/s with average turning radius 1.8 cm. (e) Snapshots of the S^{2}worm-G climbing a 1.5 × 8 mm obstacle.

TABLE VIII
SUBSTRATES ADAPTABILITY TEST OF THE S^{2}WORM-G

Substrates	Voltage (V)	Frequency (Hz)	Speed (cm/s)	Relative speed (bl/s)
Paper	220	80	54.6	13.7
	220	90	42.9	10.7
Leather	200	80	59.8	15.0
	220	80	33.3	8.3
Rubber	200	80	50.0	12.5
	220	80	41.2	10.3

The phase differences between the applied voltage and the free deflection vary with the frequencies. At a relatively lower frequency [see Fig. 12(c)], 200 V–10 Hz, the deflection is almost in phase with the driving signal. While under the 200 V–100 Hz [see Fig. 12(d)], the uprising edge of the deflection is 1.6 ms slower (16 % of a cycle) than the driving signal.

C. Speed of the Robot

Speed is one of the most important metrics for the insect-scale robot. In this section, we measure the speed of the S^{2}worm-G. The test surface is an alumina plate and the kinetic friction coefficient between the robot and the surface is 0.4. The voltage of the driving signals ranges from 160 to 220 V and the frequency ranges from 80 to 120 Hz, since the robot cannot perform steady forward locomotion above or below this range. The results of the top speed for each test are shown in Fig. 13(a). The speeds are all calculated from the 10 cm steady forward trials.

When the driving voltages are set below 200 V, the maximum speeds for each test voltage all happen at 100 Hz, and the speed at 200 V–100 Hz is 55.6 cm/s (13.9 bl/s). When the driving voltage is set as 220 V, the maximum speed happens at 90 Hz, the speed is 75.0 cm/s (18.8 bl/s) and the snapshot is shown in Fig. 13(c) [see Supplementary Movie S6]. Compared with our previous work (27.4 cm/s), the result is 2.7 times higher. This can be attributed to the efficient forward motion resulting from the resolution of the lift singularity.

The speed tests are performed with constraints to maintain the direction of the robot. If the constraints are removed, the direction of the robot can be controlled by tuning the duty cycles of the driving signals of the piezoelectric actuator decks. Supplementary Movie S6 shows that the robot can move relatively straight under the driving signal 220 V–90 Hz, duty cycle: left side-50%, right side-43%.

D. Turning of the Robot

Making turns is an important ability of the insect-scale robot in navigating and exploring tasks. The 2-DoF transmission mechanism can make turns by asynchronous actuation of the two muscle limbs. In the previous work, making turns is achieved by driving the double deck piezoelectric actuator with the same voltages but different frequencies. Specifically, if we want the robot to make a left turn and the frequency of the right deck is f_0, the frequency of the left deck is $\frac{f_0}{2}$. In this work, we adopt this method and we record the turning radius and time consumption for calculating angularity velocity and turning speed. The frequency of the right deck ranges from 80 to 120 Hz. The frequency of the left deck is set as the half of the right deck, which ranges from 40 to 60 Hz correspondingly. The voltages are set ranging from 160 to 220 V. The angular velocity and the turning radius are recorded in Fig. 13(b), and the X axis of the figure corresponds to the frequency of the right deck.

The results show that for all driving voltages under 200 V, the robot can hardly perform turning motion with a frequency of 40–80 Hz. With higher frequency combinations, the robot can always make turns smoothly except for the driving signal set as 220 V–60 Hz–120 Hz. The highest angular velocity is 2.32 rad/s with 220 V–50 Hz–100 Hz. The smallest turning radius of 1.8 cm is also under this signal [see Fig. 13(d)]. The turning test of this trial is recorded in Supplementary Movie S7.

The turning speed is defined as $angular\ velocity \times turning\ radius$. The highest turning speed is 1.98 rad/s $\times$ 4.7 cm = 9.3 cm/s with 220 V–40 Hz–80 Hz. Compared with our previous work ($\sim$1.2 cm/s), the result is 7.7 times higher. This can be attributed to the efficient turning motion resulting from the resolution of the lift and twist singularity.

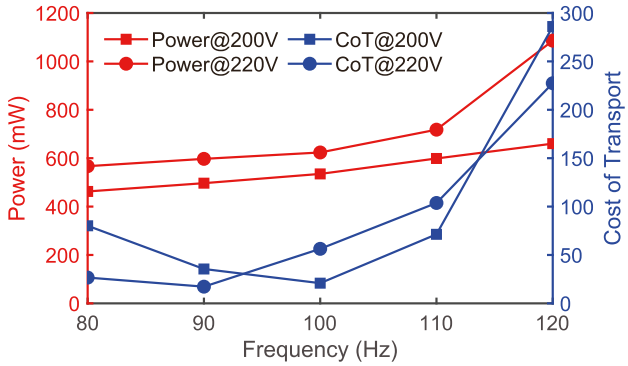

Fig. 14. Energy characterization of the S^{2}worm-G. Relationships between power and the frequency under 200 V and 220 V (red line). Relationships between the Cost of Transport and the frequency (blue line).

TABLE IX
POWER AND COST OF TRANSPORT OF THE S^{2}WORM-G

Voltage (V)	Frequency (Hz)	Speed (cm/s)	Power (mW)	Cost of Transport
220	90	75.0	597.2	17.3 (lowest)
200	100	55.6	535.0	20.9
220	80	46.1	566.9	26.7

E. Adaptability of the Robot

Adaptability allows the robot to operate in different environments. We characterize the adaptability of the S^{2}worm-G with two tests. 1) Speed test on various substrates. 2) Obstacle climbing test. (see Supplementary Movie S8)

The substrates are selected as paper, leather, and rubber. The S^{2}worm-G robot can perform steady forward locomotion on all selected substrates. The maximum top speeds and the

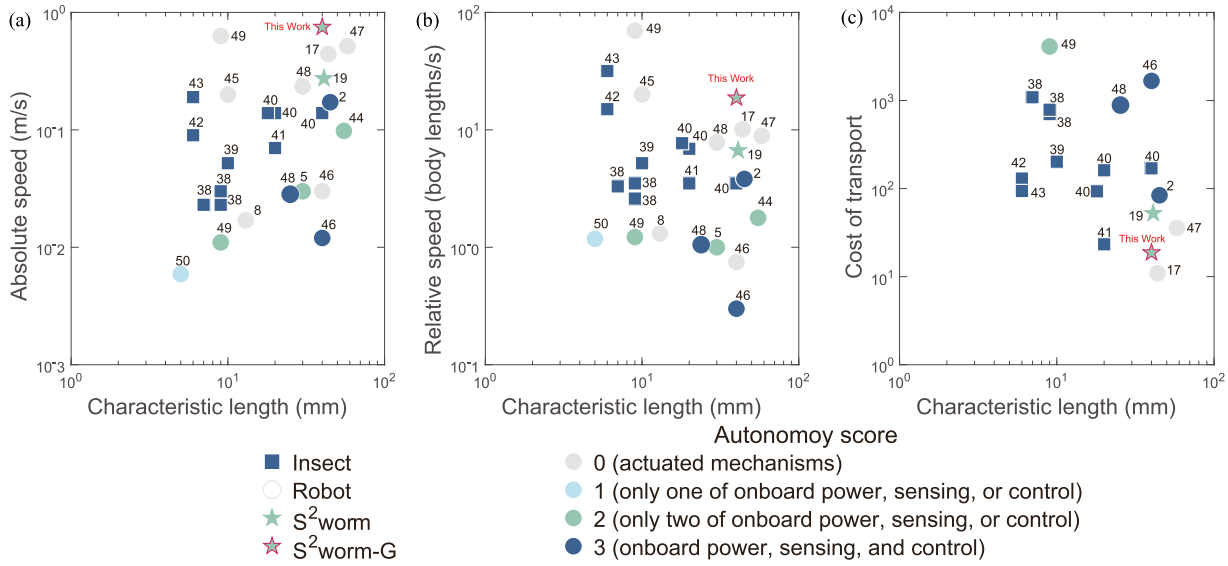

Fig. 15. Comparison of the S^{2}worm-G with some other robots and insects. The numbers on the symbols earmark the sources of references. (a) Absolute speed. (b) Relative speed. (c) Cost of transport.

corresponding test parameters are listed in Table VIII. It proves that the S^{2}worm-G can perform high speed ($\geq$ 50 cm/s, 12.5 bl/s) forward locomotion on various substrates. However, it is also observed that the frequency range is smaller for these substrates compared with the alumina plate. For example, the speed for all substrates drops sharply at over 100 Hz. We conclude that the substrates are relatively soft, and the robot is easier to stick with these substrates. Another possible explanation is that the soft substrates may absorb the small displacement of the robot during high frequency.

During the obstacle climbing test, the obstacle is selected as carbon fiber sheets with a common width (8 mm) but different heights. The driving signal is set as 220 V–90 Hz. With obstacles lower than 0.2 mm, the robot skips over the obstacle without hitting it. With obstacles higher than 0.2 mm, the robot starts to hit the obstacle which causes the speed to drop. The obstacle climbing has three steps. First, the front of the robot hits the obstacle. Then, after several cycles of hitting, the front of the robot passes the obstacle but the rear of the robot is stuck at the obstacle. Finally, the rear of the robot climb the obstacle and the robot fully passes the obstacle. The results show that the highest obstacle the S^{2}worm-G can climb is 1.5 mm, 7.6% of the robot's height. The snapshots of the trial are shown in Fig. 13(e).

F. Energy and Cost of Transport

Energy consumption of the insect-scale robot can be evaluated with the cost of transport (CoT), which is defined as $\text{CoT} = \frac{\text{Power}}{\text{Speed}\times\text{Mass}\times g}$. Where $g = 9.8$ m/s^2 is the gravity acceleration. The definition demonstrates that the CoT considers the mass of the robot.

We measure the power of the S^{2}worm-G with 200 and 220 V and the frequency ranges from 80 to 120 Hz. The results of the corresponding CoT are shown in Fig. 14. The curves show that the CoT is highly related to the speed of the robot rather than the power. Even though the power is getting higher with the increasing frequency, the velocities of the robot increase faster and the minimum CoT corresponds to the highest speed at 200 V 100 Hz and 220 V 90 Hz. The CoT of the selected tests are listed in Table IX.

G. Discussion

Fig. 15 compares this work with other robots and insects at a similar scale. We follow the metrics proposed in [11], which are: autonomy score, absolute speed, and relative speed. The autonomy score is defined as whether the robot has onboard power control and sensing devices. If none, the autonomy score is zero, if the robot has all the onboard abilities, the autonomy score of the robot is three. The autonomy scores of the natural insects are three.

Data of the insects are collected from the [38], [39], [40], [41], [42], [43]. Some recent insect-scale robots are selected as MinRAR V2 [44], Wu et al. [45], DEAnsect [46], Liu et al. [47], Liang et al. [48], SEMR TST and SEMR UL [49] and Zhu et al. [50]. Table X includes the data of this work and the selected insect-scale robots. It is shown that the S^{2}worm-G is one of the fastest insect-scale robots for its absolute speed and the relative speed. Among published reports of untethered insect-scale robots, the S^{2}worm-G holds one of the highest relative speeds. The CoT of the robot is also at the level of natural insects.

HAMR series robots have been regarded as the state of the art for almost 10 years for their high speed [17] and autonomy [2]. The developments of the HAMR also bring the SCM method to a new level and inspire a large number of microrobot projects. The S^{2}worm-G prototype we perform in this work is the second generation of the S^{2}worm project. Based on the previous work, we apply GCA to refine the SCM structure to solve the

TABLE X
COMPARISON AMONG THE S^{2}WORM-G AND SEVERAL SELECTED INSECT-SCALE ROBOTS

	Name	Size (cm)	Mass (g)	Speed (cm/s)	Relative speed (bl/s)	Cost of Transport
Tethered	SMALLbug [8]	1.3	0.03	1.7	1.3	None
	HAMR-VP [17]	4.37	1.27	44.2	10.1	11.1
	Wu et al [45]	1	0.024	20	20	None
	DEAnsect [46]	4	0.19	3	0.75	None
	Liu et al [47]	5.8	42.55	51.6	8.9	35.6
	Liang et al [48]	3	0.065	23.43	7.81	None
	SEMR TST [49]	0.9	0.17	63	70	None
Untethered	HAMR-F [2]	4.5	2.8	17.2	3.8	83.9
	RoACH [5]	3	2.4	3	1	None
	MinRAR V2 [44]	5.5	28	9.8	1.8	None
	DEAnsect [46]	4	0.97	1.2	0.3	1670
	Liang et al [48]	2.4	1.68	2.88	1.2	887
	Zhu et al [50]	0.5	0.0464	0.59	1.18	221.9
	SEMR UL [49]	0.9	0.71	1.1	1.2	4100
	S^{2}worm [19]	4.1	4.34	27.4	6.7	52.4
	This Work	4.0	4.71	75.0	18.8	17.3

singularity of the 2-DoF origami transmission mechanism we proposed. Attribute to the singularity analysis and the structure improvement, the speed of the S^{2}worm-G is 2.74 times than the previous. The high efficiency transmission mechanism makes S^{2}worm-G one of the best for its high mobility, high autonomy, and low energy consumption.

VI. CONCLUSION

In this article,we proposed a novel strategy for designing the transmission mechanism of the insect-scale robot with origami structure, that is, applying GCA to avoid the singularity of the transmission mechanism. The main contributions of this work are as follows.

1) Discovery of the inset-scale robot with SCM structure. The singularity is one of the important factors that restrict the mobility of the robot.
2) A justification for applying singularity analysis to the SCM structure.
3) The design route for refining the SCM structure with singularity analysis results.
4) A high speed untethered insect-scale robot S^{2}worm-G.

The untethered robot spans 4.0 cm in length and weighs 4.71 g. Attributed to the refined 2-DoF origami transmission mechanism, the top speed achieves 75.0 cm/s (relative speed 18.8 bl/s) for forward locomotion. As for turning motion, the angular velocity achieves 2.32 rad/s and the minimum turning radius is 1.8 cm. The maximum turning speed achieves 9.3 cm/s. The experimental results indicate that the S^{2}worm-G is one of the best insect-scale robots for its mobility, autonomy, and energy efficiency. The absolute speed and the relative speed of the S^{2}worm-G are both the highest of all untethered insect-scale robots. The robot performs high adaptability, such as moving on various substrates or climbing obstacles.

To the best of our knowledge, it is the first time to point out the importance of the singularity analysis of the transmission mechanism in the field of the insect-scale robot. It is also the first time to apply GCA in the origami transmission mechanism of the insect-scale robot to solve the singularities and improve performance. We prove that the GCA can explain the singularities of the SCM structure and help design the SCM structure to avoid singular configurations. SCM is a powerful tool in constructing miniature mechanisms and has been widely applied in insect-scale robots. This work and our previous work propose an effective route in designing the insect-scale robot fabricated by SCM, which is, designing the transmission mechanism through type synthesis and refining the transmission mechanism with GCA. Screw theory plays an important role in this route for it offers symbolic expressions during the design and analysis.

Our previous work on the BioARS system [51] has proven that a group of inchworm robots can assemble into a quadruped robot, the S^{2}worm-G is designed for constructing a BioARS system at insect scale. Besides, we will focus on the dynamic behavior of the SCM structure driven by the piezoelectric actuator for further optimization.

ACKNOWLEDGMENT

The authors would like to thank Hejinsheng Cao and Ji Tang for their help and suggestions with the PCB.

REFERENCES

[1] R. J. Wood, "The first takeoff of a biologically inspired at-scale robotic insect," *IEEE Trans. Robot.*, vol. 24, no. 2, pp. 341–347, Apr. 2008.
[2] B. Goldberg et al., "Power and control autonomy for high-speed locomotion with an insect-scale legged robot," *IEEE Robot. Automat. Lett.*, vol. 3, no. 2, pp. 987–993, Apr. 2018.
[3] Y. Chen et al., "Controlled flight of a microrobot powered by soft artificial muscles," *Nature*, vol. 575, no. 7782, pp. 324–329, 2019.
[4] C. Tang et al., "A pipeline inspection robot for navigating tubular environments in the sub-centimeter scale," *Sci. Robot.*, vol. 7, no. 66, 2022, Art. no. eabm8597.
[5] A. M. Hoover, E. Steltz, and R. S. Fearing, "RoACH: An autonomous 2.4G crawling hexapod robot," in *Proc. IEEE/RSJ Int. Conf. Intell. Robots Syst.*, 2008, pp. 26–33.
[6] Z. Zhakypov and J. Paik, "Design methodology for constructing multimaterial origami robots and machines," *IEEE Trans. Robot.*, vol. 34, no. 1, pp. 151–165, Feb. 2018.

[7] Z. Zhakypov, K. Mori, K. Hosoda, and J. Paik, "Designing minimal and scalable insect-inspired multi-locomotion millirobots," *Nature*, vol. 571, no. 7765, pp. 381–386, 2019.
[8] X.-T. Nguyen, A. A. Calderón, A. Rigo, J. Z. Ge, and N. O. Pérez-Arancibia, "SMALLBug: A 30-mg crawling robot driven by a high-frequency flexible SMA microactuator," *IEEE Robot. Automat. Lett.*, vol. 5, no. 4, pp. 6796–6803, Oct. 2020.
[9] A. Firouzeh, M. Salerno, and J. Paik, "Stiffness control with shape memory polymer in underactuated robotic origamis," *IEEE Trans. Robot.*, vol. 33, no. 4, pp. 765–777, Aug. 2017.
[10] R. J. Wood et al., "Progress on "pico" air vehicles," *Int. J. Robot. Res.*, vol. 31, no. 11, pp. 1292–1302, 2012.
[11] R. St Pierre and S. Bergbreiter, "Toward autonomy in sub-gram terrestrial robots," *Annu. Rev. Control Robot. Auton. Syst.*, vol. 2, no. 1, pp. 231–252, 2019.
[12] J. P. Whitney, P. S. Sreetharan, K. Y. Ma, and R. J. Wood, "Pop-up book MEMS," *J. Micromechanics Microeng.*, vol. 21, no. 11, 2011, Art. no. 115021.
[13] P.S. Sreetharan, J. P. Whitney, M. D. Strauss, and R. J. Wood, "Monolithic fabrication of millimeter-scale machines," *J. Micromechanics Microeng.*, vol. 22, no. 5, 2012, Art. no. 055027.
[14] D. S. Contreras, D. S. Drew, and K. S. J. Pister, "First steps of a millimeter-scale walking silicon robot," in *Proc. 19th Int. Conf. Solid-State Sensors Actuators Microsystems*, 2017, pp. 910–913.
[15] R. St Pierre, W. Gosrich, and S. Bergbreiter, "A 3D-printed 1 mg microrobot running at 15 body lengths per second," in *Proc. Solid-State Actuators Microsystems Workshop Tech. Dig.*, Hilton Head, SC, USA:Transducer Research Foundation, 2018, pp. 59–62.
[16] P. Birkmeyer, K. Peterson, and R. S. Fearing, "DASH: A dynamic 16G hexapedal robot," in *Proc. IEEE/RSJ Int. Conf. Intell. Robots Syst.*, 2009, pp. 2683–2689.
[17] A. T. Baisch, O. Ozcan, B. Goldberg, D. Ithier, and R. J. Wood, "High speed locomotion for a quadrupedal microrobot," *Int. J. Robot. Res.*, vol. 33, no. 8, pp. 1063–1082, 2014.
[18] X. Yang, L. Chang, and N. O. Pérez-Arancibia, "An 88-milligram insect-scale autonomous crawling robot driven by a catalytic artificial muscle," *Sci. Robot.*, vol. 5, no. 45, 2020, Art. no. eaba0015.
[19] Y. Liu et al., "S2worm: A fast-moving untethered insect-scale robot with 2-DoF transmission mechanism," *IEEE Robot. Automat. Lett.*, vol. 7, no. 3, pp. 6758–6765, Jul. 2022.
[20] V. Arabagi, L. Hines, and M. Sitti, "Design and manufacturing of a controllable miniature flapping wing robotic platform," *Int. J. Robot. Res.*, vol. 31, no. 6, pp. 785–800, 2012.
[21] N. T. Jafferis, E. F. Helbling, M. Karpelson, and R. J. Wood, "Untethered flight of an insect-sized flapping-wing microscale aerial vehicle," *Nature*, vol. 570, no. 7762, pp. 491–495, 2019.
[22] Y. Chen, Y. Liu, T. Liu, H. Li, S. Qu, and W. Yang, "Design and analysis of an untethered micro flapping robot which can glide on the water," *Sci. China Technol. Sci.*, vol. 65, no. 8, pp. 1749–1759, 2022.
[23] H. McClintock, F. Z. Temel, N. Doshi, J.-S. Koh, and R. J. Wood, "The milliDelta: A high-bandwidth, high-precision, millimeter-scale delta robot," *Sci. Robot.*, vol. 3, no. 14, 2018, Art. no. eaar3018.
[24] H. Suzuki and R. J. Wood, "Origami-inspired miniature manipulator for teleoperated microsurgery," *Nature Mach. Intell.*, vol. 2, no. 8, pp. 437–446, 2020.
[25] S. Mintchev, M. Salerno, A. Cherpillod, S. Scaduto, and J. Paik, "A portable three-degrees-of-freedom force feedback origami robot for human robot interactions," *Nature Mach. Intell.*, vol. 1, no. 12, pp. 584–593, 2019.
[26] M. Salerno, J. Paik, and S. Mintchev, "Ori-pixel, a Multi-DoFs origami pixel for modular reconfigurable surfaces," *IEEE Robot. Automat. Lett.*, vol. 5, no. 4, pp. 6988–6995, Oct. 2020.
[27] S. Felton, M. Tolley, E. Demaine, D. Rus, and R. Wood, "A method for building self-folding machines," *Science*, vol. 345, no. 6197, pp. 644–646, 2014.
[28] C. Gosselin and J. Angeles, "Singularity analysis of closed-loop kinematic chains," *IEEE Trans. Robot. Automat.*, vol. 6, no. 3, pp. 281–290, Jun. 1990.
[29] J.-P. Merlet, "Singular configurations of parallel manipulators and Grassmann geometry," *Int. J. Robot. Res.*, vol. 8, no. 5, pp. 45–56, 1989.
[30] P. Ben-Horin and M. Shoham, "Application of Grassmann to geometrical interpretation of parallel robot singularities," *Int. J. Robot. Res.*, vol. 28, no. 1, pp. 127–141, 2009.
[31] T. Li et al., "Agile and resilient insect-scale robot," *Soft Robot.*, vol. 6, no. 1, pp. 133–141, 2018.
[32] R. M. Alexander, *Principles of Animal Locomotion*. Princeton, NJ, USA: Princeton Univ. Press, 2006.
[33] X.-J. Liu, C. Wu, and J. Wang, "A new approach for singularity analysis and closeness measurement to singularities of parallel manipulators," *J. Mech. Robot.*, vol. 4, no. 4, 2012, Art. no. 041001.
[34] N. L. White, "Grassmann algebra and robotics," *J. Intell. Robotic Syst.*, vol. 11, no. 1, pp. 91–107, 1994.
[35] S. Amine, M. Tale Masouleh, S. Caro, P. Wenger, and C. Gosselin, "Singularity analysis of 3T2R parallel mechanisms using Grassmann algebra and Grassmann geometry," *Mechanism Mach. Theory*, vol. 52, pp. 326–340, 2012.
[36] L. L. Howell, *Compliant Mechanisms*. Hoboken, NJ, USA: Wiley, 2001.
[37] R. J. Wood, E. Steltz, and R. S. Fearing, "Optimal energy density piezoelectric bending actuators," *Sensors Actuators A: Phys.*, vol. 119, no. 2, pp. 476–488, 2005.
[38] T. F. Jensen and I. Holm-Jensen, "Energetic cost of running in workers of three ant species, Formica fusca l., Formica rufa l., and Camponotus herculeanus l. (Hymenoptera, Formicidae)," *J. Comp. Physiol.*, vol. 137, no. 2, pp. 151–156, 1980.
[39] J. R. B. Lighton, G. A. Bartholomew, and D. H. Feener, "Energetics of locomotion and load carriage and a model of the energy cost of foraging in the leaf-cutting Ant Atta Colombica Guer," *Physiol. Zool.*, vol. 60, no. 5, pp. 524–537, 1987.
[40] R. Full, D. Zuccarello, and A. Tullis, "Effect of variation in form on the cost of terrestrial locomotion," *J. Exp. Biol.*, vol. 150, pp. 233–46, 1990.
[41] J. H. Fewell, J. F. Harrison, J. R. B. Lighton, and M. D. Breed, "Foraging energetics of the ant, Paraponera clavata," *Oecologia*, vol. 105, no. 4, pp. 419–427, 1996.
[42] A. Lipp, H. Wolf, and F.-O. Lehmann, "Walking on inclines: Energetics of locomotion in the ant Camponotus," *J. Exp. Biol.*, vol. 208, pp. 707–19, 2005.
[43] L. Reinhardt and R. Blickhan, "Level locomotion in wood ants: Evidence for grounded running," *J. Exp. Biol.*, vol. 217, no. 13, pp. 2358–2370, 2014.
[44] S. A. Rios, A. J. Fleming, and Y. K. Yong, "Monolithic piezoelectric insect with resonance walking," *IEEE/ASME Trans. Mechatron.*, vol. 23, no. 2, pp. 524–530, Apr. 2018.
[45] Y. Wu et al., "Insect-scale fast moving and ultrarobust soft robot," *Sci. Robot.*, vol. 4, no. 32, 2019, Art. no. eaax1594.
[46] X. Ji et al., "An autonomous untethered fast soft robotic insect driven by low-voltage dielectric elastomer actuators," *Sci. Robot.*, vol. 4, no. 37, 2019, Art. no. eaaz6451.
[47] Y. Liu et al., "Arthropod-metamerism-Inspired resonant piezoelectric millirobot," *Adv. Intell. Syst.*, vol. 3, no. 8, 2021, Art. no. 2100015.
[48] J. Liang et al., "Electrostatic footpads enable agile insect-scale soft robots with trajectory control," *Sci. Robot.*, vol. 6, no. 55, 2021, Art. no. eabe7906.
[49] G. Mao et al., "Ultrafast small-scale soft electromagnetic robots," *Nature Commun.*, vol. 13, no. 1, 2022, Art. no. 4456.
[50] Y. Zhu et al., "A 5-mm untethered crawling robot via self-excited electrostatic vibration," *IEEE Trans. Robot.*, vol. 38, no. 2, pp. 719–730, Apr. 2022.
[51] Y. Liu et al., "BioARS: Designing adaptive and reconfigurable bionic assembly robotic system with inchworm modules," in *Proc. IEEE/RSJ Int. Conf. Intell. Robots Syst.*, 2020, pp. 11681–11687.

Yide Liu received the B.S. degree in mechatronics from Harbin Institute of Technology, Harbin, China, in 2018, and the Ph.D. degree in mechanics from Zhejiang University, Zhejiang, China, in 2023.

He is currently a Postdoctoral Researcher with the Department of Mechanical Engineering, Tsinghua University, Beijing, China. His research interests include robotic insects, multirobot system and micromanipulator.

Bo Feng received the B.S. degree in mechanical design manufacturing and automation from Yanshan University, Hebei, China, in 2019. He is currently working toward the Ph.D. degree in mechanical engineering with the Zhejiang University, Zhejiang, China.

His current research interests include mechanism design, miniature surgical robots, and control system for robot.

Tianlun Cheng received the B.S. degree in flight vehicle design and engineering from Zhejiang University, Zhejiang, China, in 2021. He is currently working toward the M.S. degree in astronautical engineering with the Zhejiang University.

His current research interests include micro air vehicle, micromechanisms, and unsteady aerodynamics.

Yanhong Chen received the B.S. degree in engineering mechanics from Zhejiang University, Zhejiang, China, in 2018. He is currently working toward the M.S. degree in solid mechanics with the Zhejiang University.

His current research interests include micro structures and micro flapping wing aerial vehicles.

Xiyan Liu received the B.S. degree in mechanical engineering from Chongqing University, Chongqing, China, in 2021. She is currently working toward the Ph.D. degree in mechanics with the School of Aeronautics and Astronautics, Zhejiang University.

Her current research interests include for nonlinear dynamics, computational neurology, bionic control for legged locomotion.

Jiahang Zhang received the B.S. degree in mechanical design manufacture and automation major from North University of China, Taiyuan, China, in 2022. He is currently working toward the M.S. degree in mechanical engineering with the Zhejiang University.

His current research interests include micro robot, reconfigurable mechanisms, shape memory alloy actuator.

Shaoxing Qu (Member) was born in Shandong, China, in 1974. He received the Ph.D. degree in mechanical engineering from University of Illinois at Urbana-Champaign, Urbana, IL, USA, in 2004.

He joined Zhejiang University, Hangzhou, China as an Assistant Professor, in 2006, and was promoted to Associate Professor, Professor in 2006 and 2011, respectively. He is currently the Qiushi Distinguished Professor with Zhejiang University, Hangzhou, China. His current research interests include intelligent robot, soft machines, and soft active materials.

Wei Yang was born in Beijing, China, in 1954. He received the Ph.D. degree in solid structure and mechanics from Brown University, Providence, RI, USA, in 1985.

He is currently a Professor with Zhejiang University, a Member of Chinese Academy of Sciences and the Head of Technological Science, a Fellow and the Treasure of The World Academy of Sciences (TWAS), a Foreign Member of National Academy of Engineering (USA). His current research interests include intelligent robot, micro/nano mechanics, mechatronic reliability, etc.